Research Article

Shuailong Lian, Wen Wan, Yanlin Zhao*, Wenqing Peng, Can Du, and Hao Hu

Study on the damage mechanism and evolution model of preloaded sandstone subjected to freezing-thawing action based on the NMR technology

https://doi.org/10.1515/rams-2024-0034 received December 07, 2023; accepted May 28, 2024

Abstract: Investigating the damage degradation of rock during the freezing and thawing process is more consistent with the actual engineering environment, considering its internal initial damage. In this study, the effects of initial damage from preloading and subzero-temperature freezing-thawing on microscopic and macroscopic mechanical properties of sandstone were studied based on the nuclear magnetic resonance (NMR) technique. The results show that the P-wave velocity of the sample decreased, while the porosity increased as the initial damage level increased. The distribution of T₂ signal intensity exposed to the low-temperature freezing-thawing-saturation treatment was rather larger than that under normal temperature conditions for samples with different levels of initial damage from preloading, indicating that the low-temperature freezing-thawing condition would promote the porosity and have an obvious increase in damage. A continuum damage model considering subzero-temperature freezing-thawing damage from different pore sizes was finally introduced to describe the damage evolution mechanism of sandstone. The research results can be used to quantitatively evaluate the damage evolution mechanism of sandstone treated by subzero-temperature freezing—thawing without mechanical tests. Furthermore, the analysis and research results show that the damage variables of sandstone obtained by the NMR theory were lower than those of classical rock mechanics theory.

Keywords: preloaded sandstone, nuclear magnetic resonance, freezing—thawing damage model

1 Introduction

Rock materials in the development of mineral resources and construction of civil engineering are easily affected by seasonal and diurnal temperature cycles in cold areas. Investigating the freezing-thawing mechanical properties of rock is of great significance for geotechnical engineering in cold regions [1-5]. Deterioration of mechanical properties depends on the internal damage of rock. The internal damage of rock is closely related to the change of the microscopic pore structure. A majority of researchers coming from various scientific fields have made significant contributions to the current knowledge about this question [6–10]. The internal damage of rock lies in the manner by which subzero temperatures changed the microscopic pore structure, but it has not been obviously confirmed. In addition, microscopic pore structures affect the unfrozen water contents and other properties. Therefore, studying and understanding the freezing-thawing damage mechanism and evolution model of sandstone is the basis for revealing the mechanism of freezing-thawing damage in geotechnical engineering [11-15].

Moreover, most previous studies pay a great attention to quantifying the frost-heave strain and the corresponding frost damage evolution mechanism of intact rock during freezing. Lithology, porosity, water saturation, number of freezing—thawing cycles, freezing—thawing cycle temperature and rate, hydration environment, unfrozen water

Shuailong Lian: School of Resources Environment and Safety Engineering, Hunan University of Science and Technology, Xiangtan, Hunan 411201, China; College of Civil Engineering, Guizhou University, Guiyang, Guizhou 550025, China

Wen Wan, Wenqing Peng: School of Resources Environment and Safety Engineering, Hunan University of Science and Technology, Xiangtan, Hunan 411201, China

Can Du, Hao Hu: College of Civil Engineering, Guizhou University, Guiyang, Guizhou 550025, China

^{*} Corresponding author: Yanlin Zhao, School of Resources Environment and Safety Engineering, Hunan University of Science and Technology, Xiangtan, Hunan 411201, China, e-mail: zhaoyanlinhnust123@163.com

content and stress state, and freezing times have been regarded as major factors influencing the mechanical properties of rocks [16–30]. However, the change of phase composition of pore water in porous rock is a direct index of the freezing–thawing process of rock. It is usually estimated by measuring the water content against temperature under different freezing–thawing conditions, obtaining the pore distribution, and analyzing the freezing–thawing damage [31–33].

A majority of detection methods and technology were also adopted to reveal the change of phase composition of pore water, and the internal cracking process of the sample is from the microscopic to macroscopic during the progress of freezing—thawing [34–40]. The nuclear magnetic resonance (NMR) method is a better choice for studying the freezing mode of pore water in complex pore structures at low temperatures. The composition of pore water can be deduced according to the T₂ spectrum of pore water in different pore structures, and the changes in each component during freezing can provide a more detailed pore water freezing mode. This method has a good prospect to evaluate the pore distribution of geotechnical materials, to measure the content of water, and to estimate rock freezing—thawing damage in cold regions [41–46].

Currently, scholars have provided many meritorious research achievements illuminating freezing-thawing damage characteristics of rocks caused by a complicated freezingthawing environment, but most research works place a particular emphasis on intact rock, and there are few studies on the damage characteristics during the freezing-thawing process of rock with different initial damage conditions [47-55]. In practical applications, initial damage is an important problem to be considered in the freezing-thawing test. In the construction process, the basic mechanical rock breaking method is usually adopted for slope, tunnel, culvert, and other rock engineering, which would inevitably cause different damage levels to the engineering project in cold regions [56–60]. The change of the macroscopic mechanical properties of rock mainly depends on the degree of freezing-thawing action on the internal structure of rock. The ineluctable initial damage exacerbates the effects of freezing-thawing. The initial damage corresponds to the weak structural surface in the rock. Rock disintegration occurs along the weak structural plane under loading conditions, and different initial damage levels change the rock failure mode [61–65].

In fact, it is more suitable for the actual engineering environment and engineering conditions to investigate the deterioration characteristics of freezing—thawing damage, considering the internal damage of rock mass, and the results have more practical value for the evaluation of geotechnical engineering safety in cold regions. In this study, the NMR technique was used to study the freezing—thawing

process of pore water in sandstone samples with various levels of initial damage from preloading (0, 0.3, 0.5, 0.7, and 0.9 of the ultimate uniaxial compressive strength [UCS]) under different temperature conditions (25, 0, -5, -10, -15, and -20°C). Various levels of initial damage were fabricated by previous preloading (loading and unloading) to various preset stresses, and the pore structures of saturation sandstone samples with various levels of initial damage were measured using the NMR technique under five subzero-temperature freezing-thawing process. The T₂ spectrum distribution, T₂ spectral area, and the evolution of pore structure were obtained for the sample with various levels of initial damage during the freezing-thawing process. A continuum damage model considering subzero-temperature freezingthawing damage from different pore sizes is finally introduced to describe the damage evolution of sandstone with various levels of initial damage under the five subzero-temperature freezing-thawing process. Finally, the UCS test was carried out on samples after low-temperature freezing-thawing.

2 Experimental scheme

2.1 Sample preparation

The red sandstone samples were collected from the Linyi County, Yunnan Province, China. X-ray analysis showed that the main components of samples were quartz (59%), feldspar (18%), calcite (13%), and kaolinite (10%) (Figure 1). Three standard cylindrical sandstone samples with the dimensions of 50 mm in diameter and 100 mm in length were prepared to evaluate the UCS. For the purpose of obtaining reliable test results, the UCS of the samples was

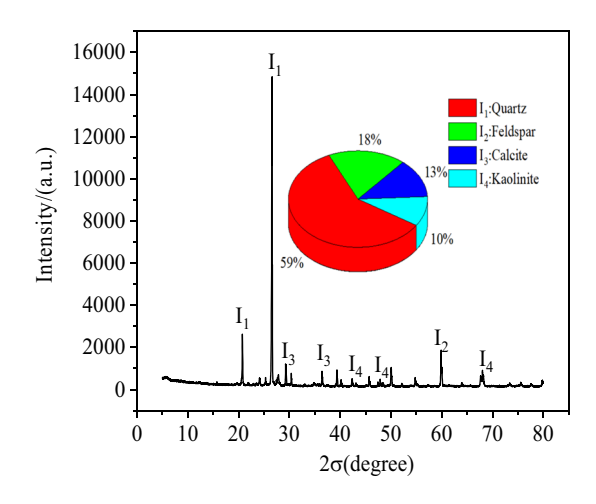


Figure 1: X-ray diffraction pattern.

Table 1: Physical and mechanical parameters of sandstone

Туре	ρ (kg·m ⁻³)	V _p (km·s ⁻¹)	n (%)	ω ₀ (%)	E _s (GPa)	μs	UCS (MPa)
Red sandstone	2,483	2.472	4.32	2.58	16.37	0.32	78

Note: ρ – mass density; V_p – P-wave velocity; n – porosity; ω_0 – moisture content; E_s – elastic modulus; μ_s – Poisson's ratio; UCS – unconfined compressive strength.

determined by the average value of the UCS of the three samples. The T₂ spectrum was obtained from ten saturated samples, of which five samples were selected to produce the levels of initial damage (0, 0.3 (30%), 0.5 (50%), 0.7 (70%), and 0.9 (90%) of the ultimate UCS) by previous preloading (loading and unloading). Therefore, a total of 13 samples were adopted in this study (Table 1).

2.2 Test facilities

The NMR equipment from the Suzhou Niumag Analytical Instrument Corporation (MacroMR12-150H-I) was used in this experiment, as shown in Figure 2. The T₂ distribution and NMR images of test samples during the freezing process can be obtained by using the Core Analysis software. The NMR device has a magnetic field strength of 0.3 T, which can measure the T₂ distribution. The Carr-Purcell-Meiboom-Gill sequence was used to measure the T2 distribution. The pulse duration was set as 11 µs, the echo time as 0.2 ms, and the delay between scans as 2,000 ms. For the purpose of ensuring the best operation of the test system and the accuracy of the test results, the room temperature required for the test is 20-25°C. The diagram of the experimental system and procedure is shown in Figure 2.

2.3 Setup of experiments

The test process includes the freezing-thawing test, the NMR test, and the UCS test. The test procedure is illustrated in Figure 3. The specific steps are as follows.

- 1) Samples were dried at 105°C for 24 h in the drying box, weighing its mass. Three samples were loaded until failure, and their average UCS was 78 MPa. The UCS was a reference stress used to determine the unloading point. Accordingly, five groups of samples were prepared and preloaded to various preset stress levels followed by unloading to zero. Figure 4 presents the loading and unloading paths, where the preloading levels were predefined to be 0, 0.3, 0.5, 0.7, and 0.9 UCS at 0.5 MPa·min⁻¹ for five groups of samples. Table 2 lists the preloading stresses and the corresponding loading ratios (loading levels over the UCS) [59]. The initial damage (k) is described as the ratio of preloading stress to UCS [62]. In addition, the Pwave velocity and porosity before and after the initial damage were measured to prove that the sample did indeed generate initial damage by previous uniaxial loading and unloading tests.
- Samples with different initial damage were vacuumed at 0.1 MPa pressure for 6 h in a vacuum-saturated facility. Then, the internal pores were completely saturated with water at a pressure of 20 MPa for 24 h.



Figure 2: NMR test system (model, MacroMR12-150H-I).

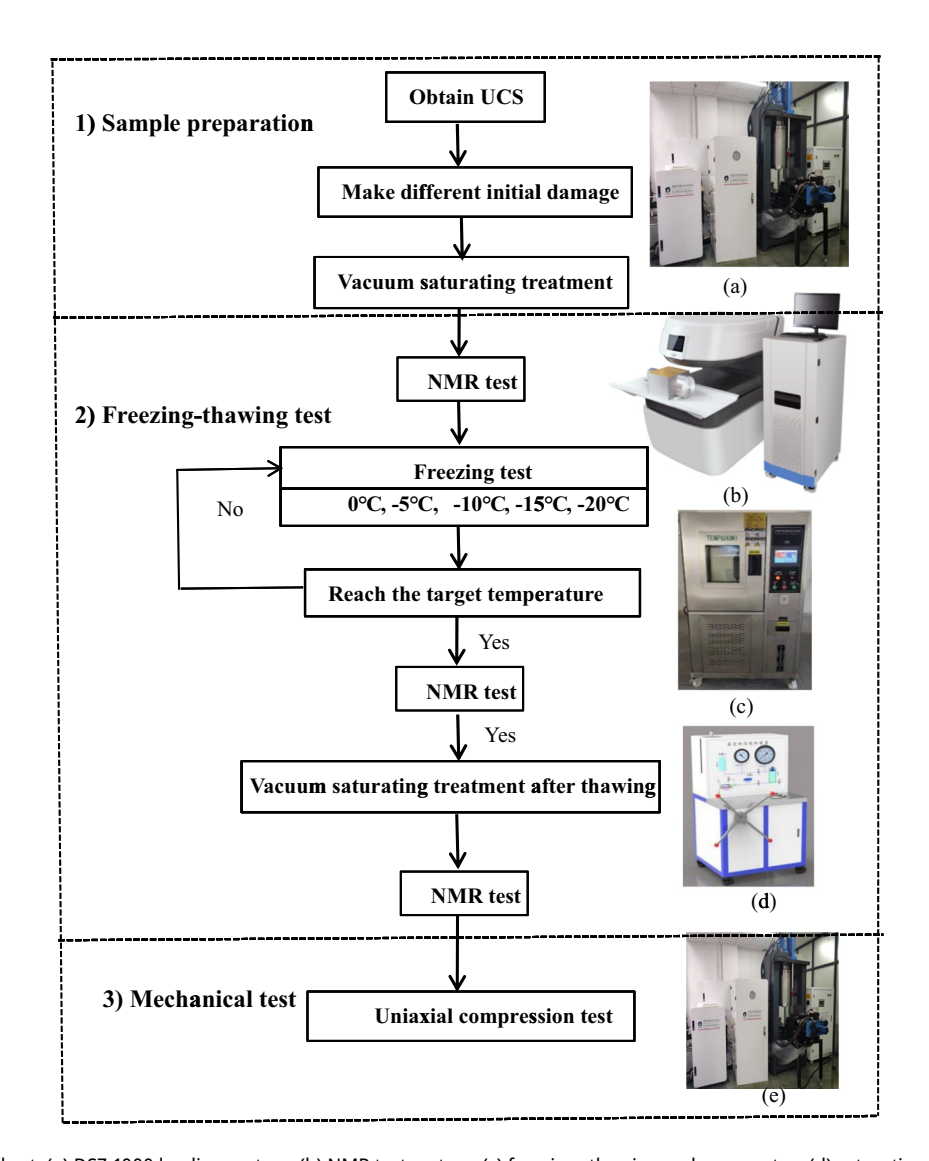


Figure 3: Test flow chart: (a) DSZ-1000 loading system, (b) NMR test system, (c) freezing–thawing cycle apparatus, (d) saturation water device, and (e) DSZ-1000 loading system.

- 3) Completely saturated samples with different levels of initial damage were put into a programmable test chamber at −20 to 25°C and the saturated samples were frozen from room temperature to various temperature levels (25, 0, −5, −10, −15, and −20°C). The ambient temperature deviation of the chamber was controlled within ±0.2°C. A total of six temperature levels were set during the freezing process, as shown in Figure 5. The samples were maintained for 6 h to achieve thermal equilibrium at each temperature level. The NMR detection was conducted at each temperature level under freezing—thawing conditions. The results of NMR tests included the porosity, T₂ spectrum distribution, and T₂ spectral area at various temperature levels.
- 4) Steps 2 and 3 were conducted on the samples after the completion of the 0, -5, -10, -15, and -20°C freezing-

thawing. The UCS tests were performed on the samples at a 0.5 MPa·min⁻¹ rate that had been exposed to different freezing—thawing temperatures.

2.4 Validation of NMR tests

Yang *et al.* verified the precision of the NMR porosity measurements using traditional weighting methods [44]. In this article, the traditional weighting method was used to prove its accuracy. The porosity acquired from the traditional weighting method was determined by the following equation:

$$\rho_{\rm c} = (m_{\rm s} - m_{\rm d})/\rho_{\rm w} v_{\rm s}, \tag{1}$$

where ρ_c is the porosity tested by the traditional weighting method, m_s is the saturated mass, m_d is the dry mass, ρ_w is

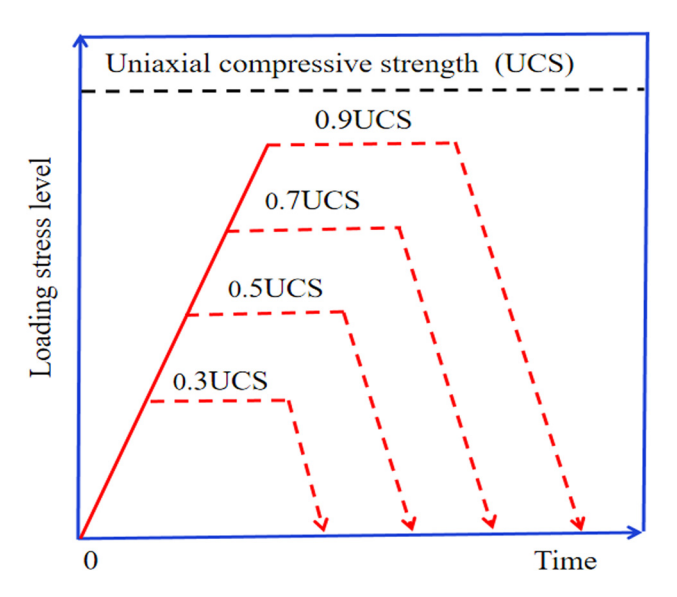


Figure 4: Loading/unloading paths for compression tests.

the density of water, and v_s is the volume, which were calculated from the dimensions of saturated sample.

To validate the effectiveness of the NMR test, it is significant to make a comparison to the porosity values acquired from conventional measurements and the NMR test. For this reason, the porosities obtained by using the NMR experiments and the weighting methods are shown in Table 3, respectively. The results demonstrate that the porosity measured by NMR was fairly smaller than that measured by the weighting method. This deviation is due to the restriction of the NMR technique. NMR is generally unable to monitor pores smaller than 3 nm due to the extremely fast volatilization of hydrogen in small pores [45]. Nevertheless, the discrepancy between the NMR porosity and the conventional porosity is relatively small (no more than 3%), which would not significantly affect the results of the subsequent NMR test.

3 Experimental results

3.1 Changes in the porosity and P-wave velocity before and after preloading

The changes in the P-wave velocity and porosity before and after initial damage are presented in Figure 6. With the

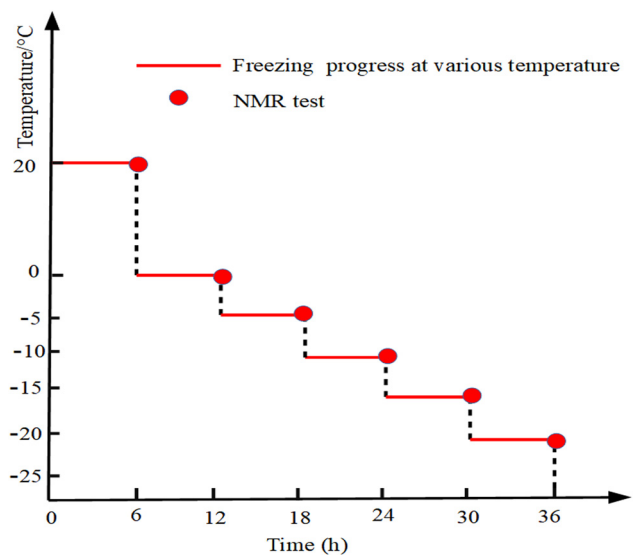


Figure 5: NMR tests at various temperature levels during the freezing process.

Table 3: Comparison of the NMR porosity with the conventional porosity

Samples (%)	Initial damage	NMR porosity (%)	Conventional porosity (%)	Error (%)	
S-1-0	0	4.32	4.36	0.9	
S-2-30	0.3UCS	4.46	4.51	1.1	
S-3-50	0.5UCS	4.62	4.70	1.7	
S-4-70	0.7UCS	4.98	5.08	2.0	
S-5-90	0.9UCS	5.18	5.32	2.6	

increase of the initial damage level, the P-wave velocity of the sample decreases, while the porosity increases, which prove that initial damage is indeed generated by uniaxial loading and unloading of the sample. In addition, the P-wave velocity and porosity change rate show an obvious inflection point when the initial damage is 50%, and the rate of change on the left side is much smaller than that on the right side. This change is mainly due to the initiation of crack coalescence at this stress level, which is about 0.5–0.7 times the peak strength [66]. Therefore, under the loading of 0.5UCS or higher, the crack merging or joining in the sample is the cause of the sudden increase of porosity and the sudden decrease of P-wave velocity.

Table 2: Preload stress (MPa)

Samples	S-1-0	S-2-30%	S-3-50%	S-4-70%	S-5-90%	
Initial damage (k)	0	0.3 (30%)	0.5 (50%)	0.7 (70%)	0.9 (90%)	UCS
Stress	0	26	39	55	70	78

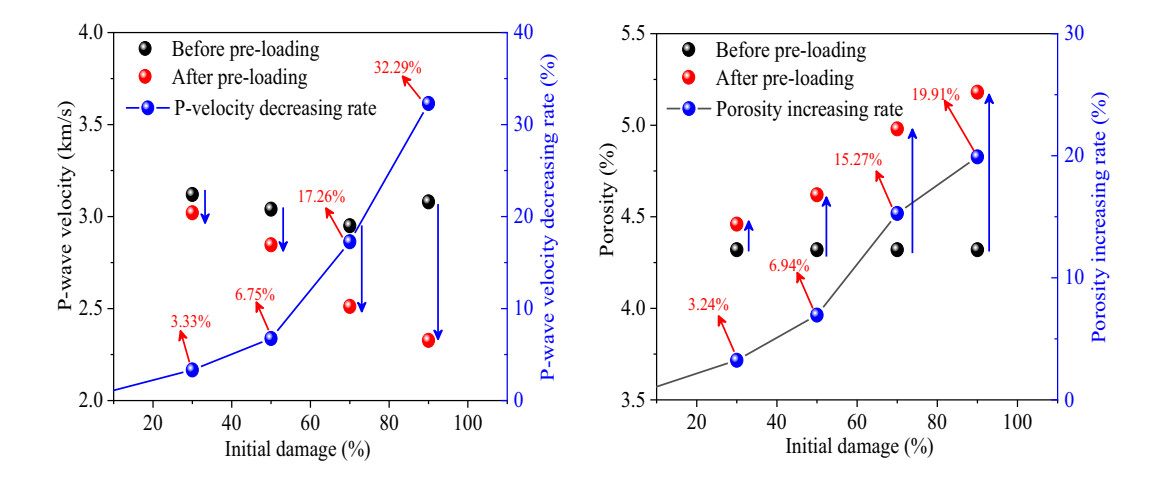


Figure 6: Changes in the P-wave velocity and porosity against the initial damage level.

The changes in P-wave velocity and porosity were in good agreement, both of which indicate the accumulation of damage and material deterioration with the increase of the initial damage level.

3.2 Changes in the T₂ distributions before and after preloading

 T_2 is a time constant for the exponential decay of the magnitude of a spin echo for a single pore body [67]. For a multiple pore body system such as a porous network, the exponential decay is a summation of individual decays. Using an inversion-processing technique, the raw decay curve can be fitted to a T_2 spectrum. Most of the NMR interpretations and estimated physical parameters are based on this T_2 spectrum [68]. The T_2 distribution of the

samples can be mainly divided into three peaks, as shown in Figure 7, corresponding to the transverse relaxation time T_2 spectrum of micro-pores (0.01–1 ms), meso-pores (1–100 ms), and macro-pores (100–1,000 ms) from left to right [23,69].

Figure 7(a) and (b) shows the T_2 spectrum distribution of samples before and after different levels of initial damage by preloading, respectively. Before the initial damage, the peak areas of the micro-pores and the macro-pores of the five tested samples were basically the same, while there were only a few differences in the peak areas of the meso-pores. After the initial damage by post-loading, the peak area of the micro-pores and the meso-pores increased as the initial damage increased, especially for the peak areas of the meso-pores, and the changes were particularly dramatic. The peak area of the macro-pores did not change obviously before the degree of damage reached 90%, but the area increased suddenly when the initial damage was 90%.

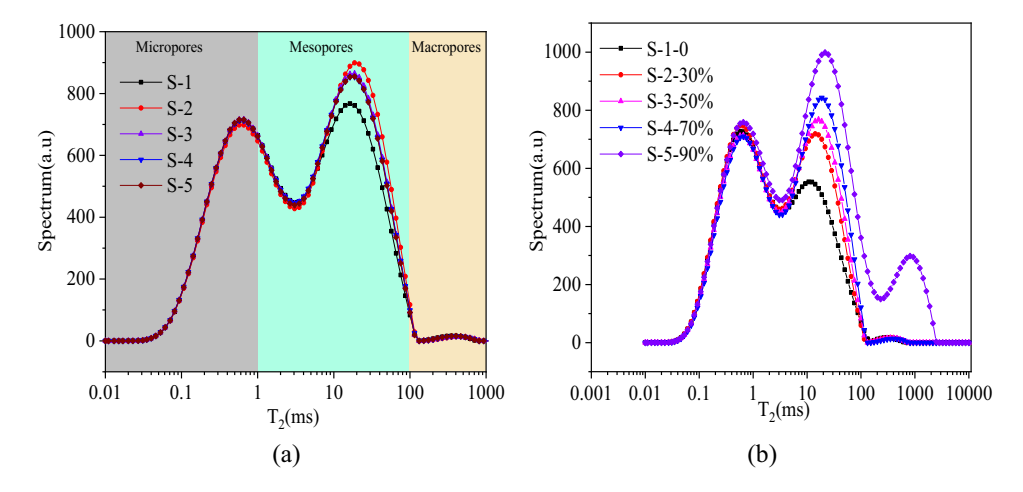


Figure 7: T₂ spectrum distribution curves of the five samples: (a) pre-loading initial damage and (b) post-loading initial damage.

3.3 T₂ distributions with freezing progression

Figure 8 displays the T_2 distribution of the samples under low-temperature conditions of 25, 0, -5, -10, -15, and -20° C with different levels of initial damage by preloading. There were three obvious peaks, which were obviously different from the maximum signal intensity of the three peaks of all

test samples, indicating different energy states of pore water and the corresponding pore water quantity. In the case of same levels of initial damage, the water in the pores froze, and the peak value dropped rapidly as the temperature decreased. When the freezing temperature reached -15°C, the peak value dropped gently. When the freezing temperature reached -20°C, the signal intensity of the meso-pores gradually approached 0.

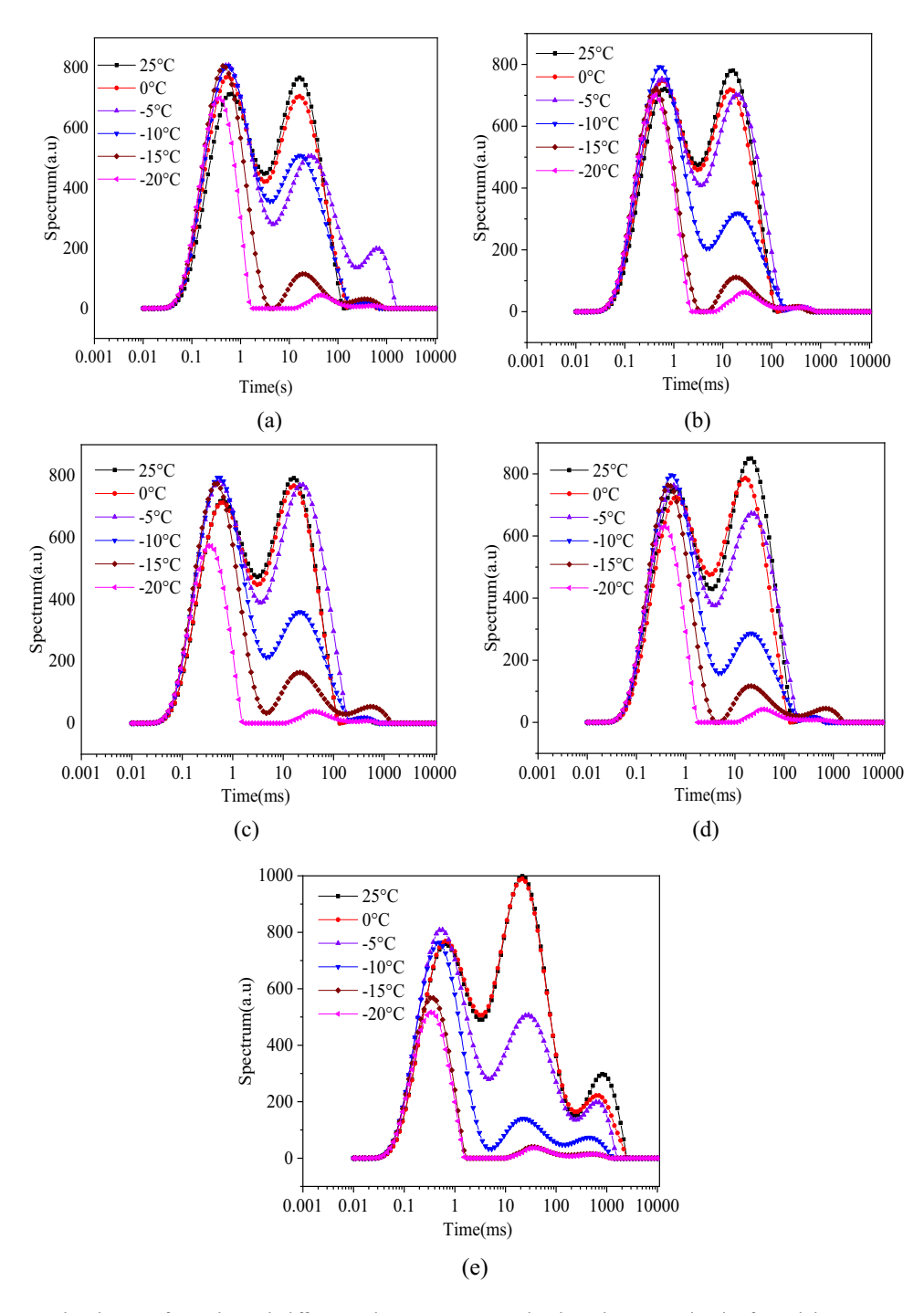


Figure 8: T₂ spectrum distribution of samples with different subzero temperature levels under various levels of initial damage: (a) 0 UCS, (b) 0.3 UCS, (c) 0.5 UCS, (d) 0.7 UCS, and (e) 0.9 UCS.

Figure 9 shows that the T_2 distribution of samples with different levels of initial damage from preloading is obvious at 25, 0, -5, -10, -15, and -20°C. There were also three obvious peak values, which were significantly different from the maximum signal intensity of the three peaks of all test samples, indicating different energy states of pore water and corresponding pore water quantities. At the same

temperature (25 and 0°C), the peak signal intensity of the micro-pores, meso-pores, and macro-pores increased as the levels of initial damage increased. However, below 0°C, especially after -5°C, when the water in the pores froze, the peak signal intensity of the micro-pores, meso-pores, and macro-pores decreased continuously, and the decline of the micro-pores and the meso-pores was the most obvious.

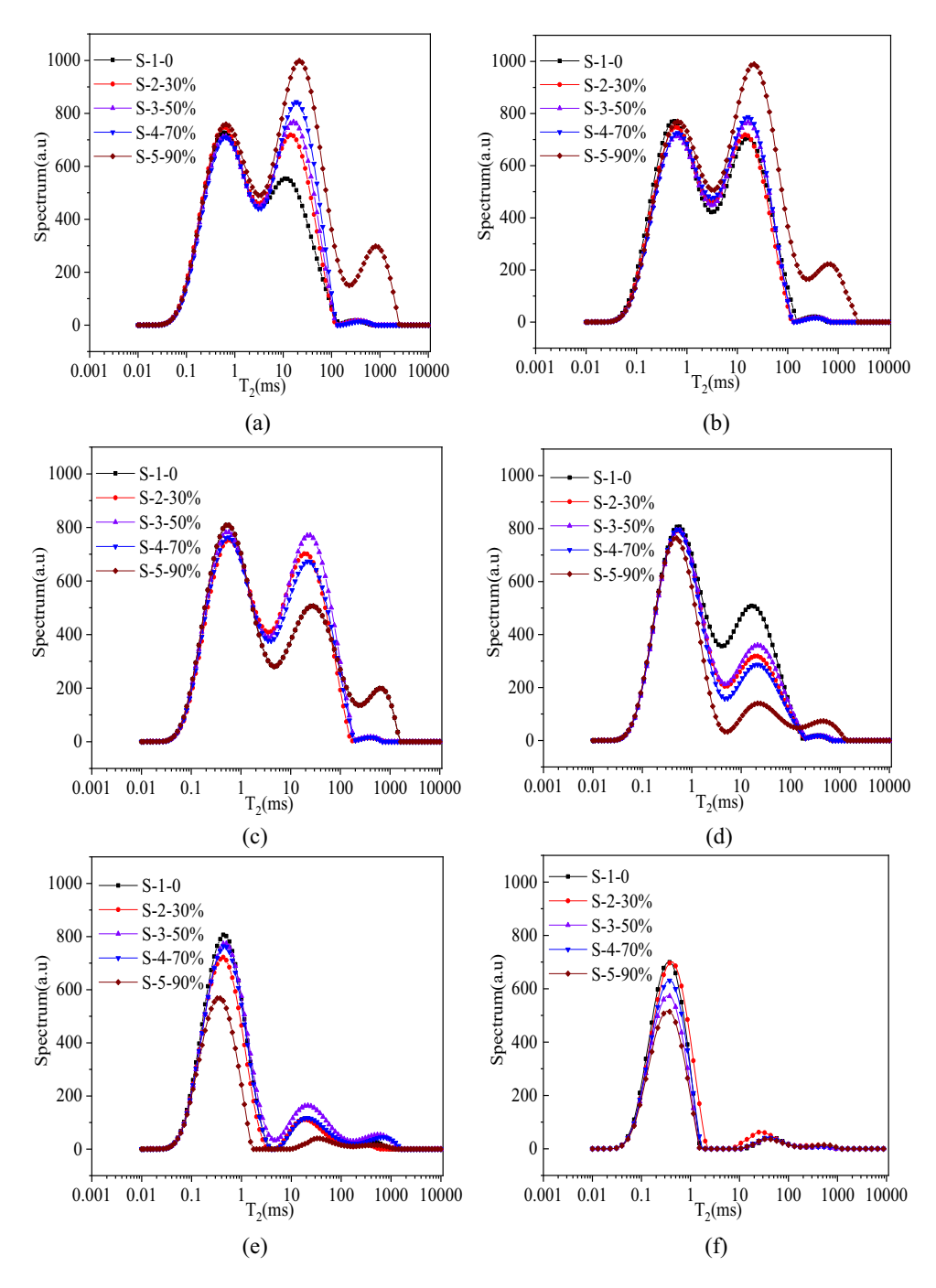


Figure 9: T_2 spectrum distribution of samples with different levels of initial damage under various temperature levels. (a) 25°C, (b) 0°C, (c) -5°C, (d) -10°C, (e) -15°C, and (f) -20°C.

3.4 T₂ distributions with thawing progression

For samples with different levels of initial damage, which were put into water to allow natural melting and return to normal temperature after a gradient of low-temperature treatment of 0, -5, -10, -15, and -20° C at each temperature gradient drop. Then, the samples were subjected to vacuumpressure treatment and saturated with water for 24 h. After that, T₂ was detected by NMR technology. The T₂ distribution after freezing-thawing-saturation was obtained according to the above process. For all samples at each temperature gradient drop, freezing-thawing-saturation-T₂ was measured. The T₂ distribution curve of the saturated samples before freezing and after thawing basically does not change at temperatures of 0 and -5°C. Therefore, the T₂ distribution curves of freezing-thawing-saturation are not listed at the temperatures of 0 and -5°C. Figure 10 illustrates that the peak of T₂ is bigger than without treated with low-temperature or room-temperature conditions when the initial damage was 0-70%; the freezing-thawing-saturation-measured T₂ distribution peak area increased gradually as the freezing temperature declined, but the macro-pores did not change. For samples with an initial damage level of 90%, the changes in the micro-pores and the meso-pores were not obvious, but the macro-pores have an obvious change. For samples with different levels of initial damage from preloading, the distribution of T2 signal intensity after low-temperature freezing-thawing-saturation treatment was rather larger than that under normal-temperature conditions, showing that the porosity of the samples increased at low-temperature freezing-thawing conditions, which promoted further damage for the sample containing different levels of initial damage. Because the pores of the samples increased after freezing-thawing damage, the peak value of T₂ increased after saturation at low-temperature conditions.

Figure 11 shows the T₂ distribution of different levels of initial damage after freezing-thawing-saturation at -10, -15, and -20°C. The larger the levels of initial damage, the larger the T2 peak value obtained after freezingthawing-saturation treatment at a low temperature. The change of micro-pores was not obvious, the peak value showing an increasing trend, and the change of the mesopores was particularly obvious, and it was mainly divided into two obvious growth stages, the levels of initial damage were from 0 to 70% and the levels of initial damage were from 70 to 90%, and the peak value of the meso-pores increased rapidly.

3.5 T₂ spectral area with freezing progression

The T₂ distribution peak area changes of the micro-pores, meso-pores, and macro-pores after various low temperatures obtained by NMR testing are indicated in Figure 12 for samples with various levels of initial damage from preloading. The results suggested that the pore areas of the micro-pores, meso-pores, and macro-pores increased as the temperature decreased. This is because that the low temperature freezing caused the number of micropores for the tested samples, and the micro-pores were expanded and connected to form the meso-pores and macro-pores, indicating that the low temperature would cause damage and destroy the samples. Figure 12 shows that the growth rate of pore area of has three stages: the first stage was 25 to -5°C, the second stage was -5 to -15°C, and the third stage was -15 to -20°C. The low temperature also would cause the free water to frost-heaving and freezing-thawing repeatedly for the sample with different levels of initial damage. The micro-pores developed rapidly, which was demonstrated as an obvious change rate at the temperature of -10°C. This is the reason that low-temperature freezing causes the pore size to expand and extend, making a lot of new micro-pores. But after -15°C, the growth rate of pore area of the micro-pores slowed down, showing a rapid decline, and this is the reason that micro-pores continue to extend and develop into meso-pores dramatically. Conversely, the meso-pores decreased rapidly at temperature levels from -5 to -15°C, and this is the reason free water freezes due to low temperature, causing the area of the meso-pores to be filled with ice. The meso-pores increased sharply at temperature levels from -15 to -20°C, and this is the reason that low temperature causes new micro-pores continue to extend and develop into meso-pores dramatically.

For samples exposed to the low temperature levels of 25, 0, -5, -10, -15, and -20°C, T_2 distribution peak areas of three pore changes at various initial damage levels obtained by NMR testing are shown in Figure 13. At a temperature of 25°C, the T₂ distribution peak area of the micro-pores gradually increased and the meso-pores gradually decreased before the initial damage levels of 50%. Conversely, the T₂ distribution peak area of the micro-pores gradually decreased and the meso-pores gradually increased after the initial damage levels of 50%. The T₂ distribution peak area of the macro-pores shows no obvious change before the initial damage levels of 70%. At a temperature of 0°C, the T₂ distribution peak area of the micro-pores gradually increased and

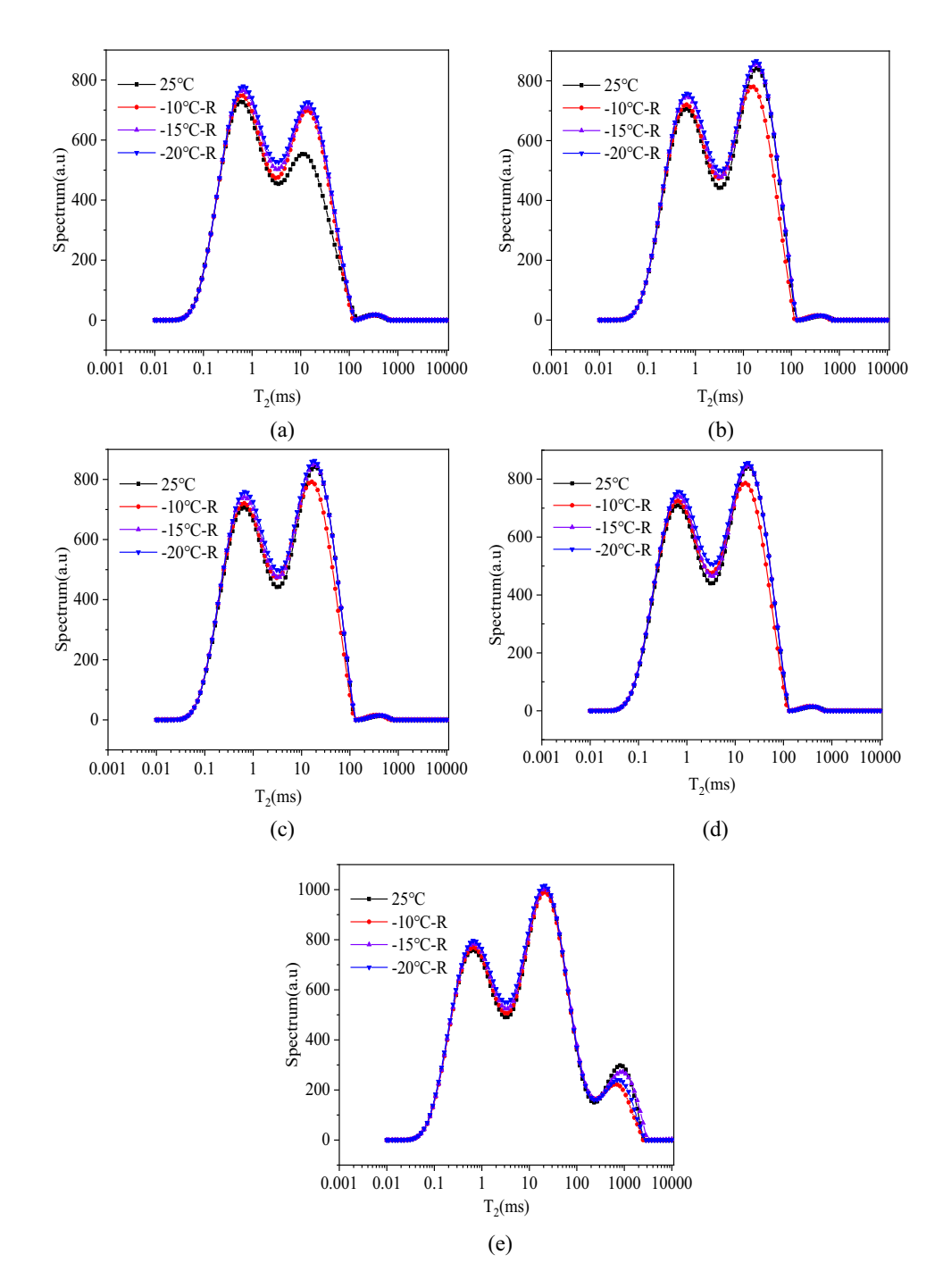


Figure 10: T_2 spectrum distribution of samples with various temperatures under different levels of initial damage: (a) 0 UCS, (b) 0.3 UCS, (c) 0.5 UCS, (d) 0.7 UCS, and (e) 0.9 UCS. R stands for thawing and -10° C-R represents the sample after -10° C freezing–thawing–saturation.

the meso-pores gradually decreased before the initial damage level of 30%. Conversely, the T_2 distribution peak area of the micro-pores gradually decreased and that of the meso-pores gradually increased after the initial damage levels of 70%. At the initial damage levels from 30 to 70%, the T_2 distribution peak areas of micro-pores and meso-pores show no distinct difference. The T_2 distribution peak area of the macro-pores

shows no obvious change in the initial damage levels from 0 to 90%. At a temperature of -5° C, the T_2 distribution peak area of the micro-pores gradually increased and that of the meso-pores gradually decreased before the initial damage level of 70%. Conversely, the T_2 distribution peak area of the micro-pores gradually decreased and that of the meso-pores gradually increased after the initial damage level of

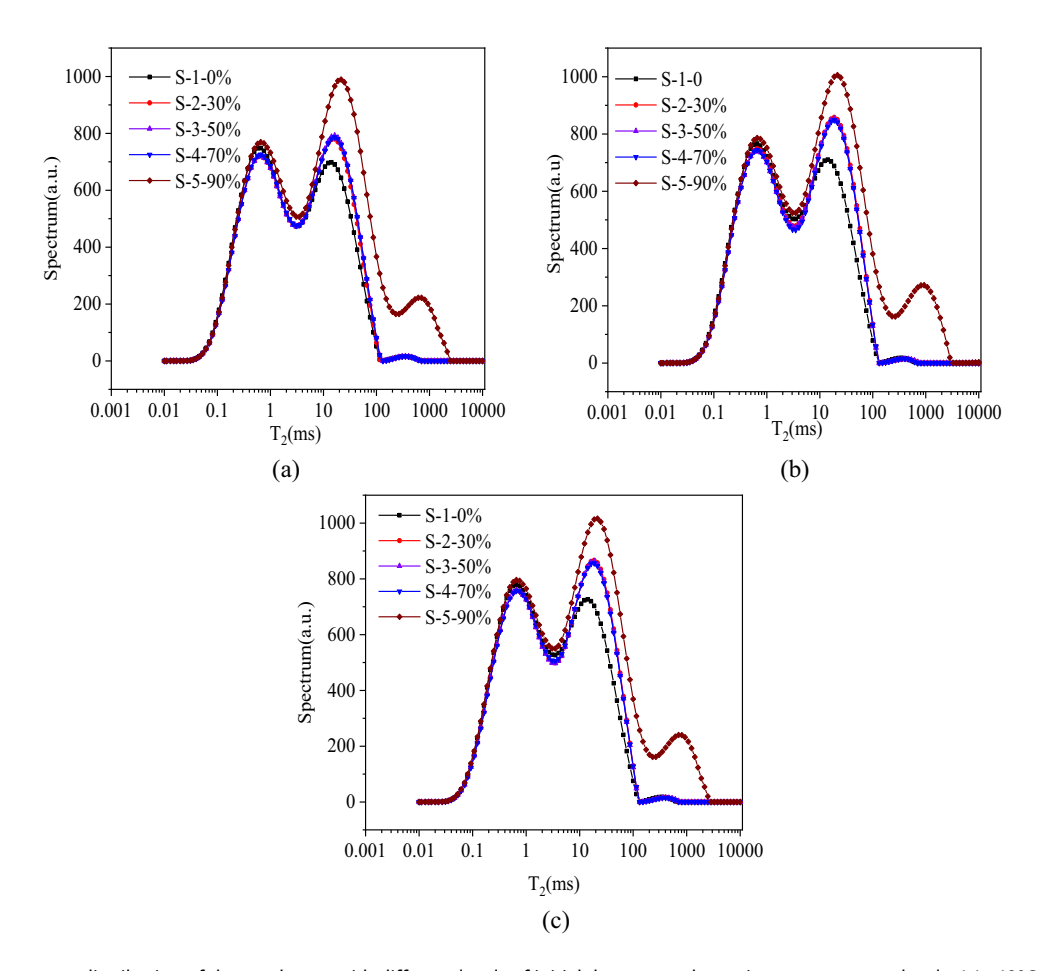


Figure 11: T_2 spectrum distribution of the sandstone with different levels of initial damage under various temperature levels: (a) -10° C-R, (b) -15° C-R, and (c) -20° C-R.

70%. The T₂ distribution peak area of the macro-pores first decreased at the initial damage level of 30% and then gradually increased at the initial damage level from 30 to 90%. At a temperature of -10°C, the T₂ distribution peak area of the micro-pores gradually increased and that of the meso-pores gradually decreased at the initial damage levels from 0 to 90%, and the T₂ distribution peak area of the macro-pores showed no obvious change before the initial damage level of 70%. At a temperature of -15° C, the T_2 distribution peak areas of the micro-pores and the macro-pores gradually decreased and that of the meso-pores gradually increased before the initial damage level of 50%. Conversely, the T₂ distribution peak area of the micro-pores and the macro-pores gradually decreased and that of the meso-pores gradually increased after the initial damage level of 50%. At a temperature of -20°C, the T₂ distribution peak area of the micro-pores and the meso-pores shows no distinct change at the initial damage levels from 0 to 90%. The T2 distribution peak area of the macro-pores gradually decreased before the initial damage level of 70% and it increased after the initial damage level of 70%.

3.6 T₂ spectral area with thawing progression

For the samples exposed to different levels of initial damage (0, 30, 50, 70, and 90%) from preloading, the T_2 distribution peak areas of three pore changes after various low-temperature freezing—thawing—saturation obtained by the NMR testing are shown in Figure 14. It can be found from Figure 14 that the quality of the micro-pores, meso-pores, and macro-pores shows no obvious difference for 0, 30, and 90% initial damage levels. But the quality of the micro-pores, meso-pores, and macro-pores shows a marked change for 50 and 70% initial damage levels.

For samples with initial damage of 0%, the total pore area of the three pore sizes increased with the decrease in temperature after freezing and thawing at different low temperatures. The areas of the micro-pores and the mesopores show an obvious upward trend, while the area of the macro-pores did not alter significantly.

For samples with an initial damage of 30%, the total pore area of the three pore sizes decreased first and then increased with the decrease in temperature for samples with different

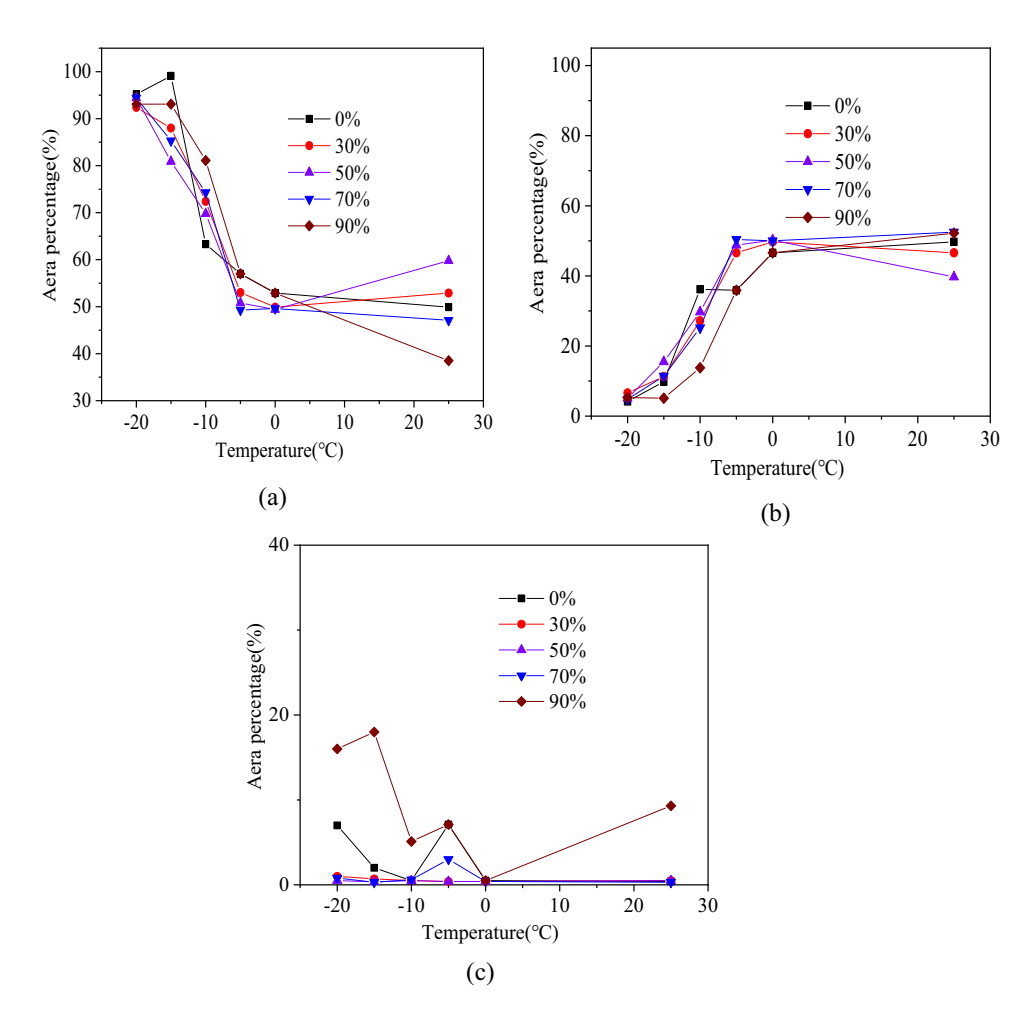


Figure 12: Relationship between the area of the spectral peak and the temperature during the process of freezing: (a) first spectral peak, (b) second spectral peak, and (c) third spectral peak.

freezing–thawing–saturation conditions, and the area of micropores increased monotonically. The area of meso-pores to reduce (25 to -10° C) after adding (-10 to -15° C) to minimize (-15 to -20° C), the area of macro-pores, first increase (25 to -10° C) after decreased (-10 to -15° C) and add (-15 to -20° C).

For samples with an initial damage of 50%, with the decrease of temperature, the total pore area of the three kinds of pores first decreased and then increased; the area of micro-pores first decreased (25 to -10° C), and then increased (-10 to -20° C); the area of meso-pores increased monotonically, and the area of macro-pores first decreased (25 to -15° C) and then increased (-15 to -20° C).

For samples with 70% initial damage, the total pore area of the three kinds of pores first decreased and then increased with the decrease of temperature for the sample with different low-temperature freezing–thawing–saturation conditions, and the area of micro-pores increased monotonically. The area of the mesopores reduced (25 to -10° C) after an increase (-10 to -20° C), and the area of macro-pores first increased (25 to -10° C), followed by a decrease (-10 to -15° C) and then increase (-15 to -20° C).

For samples with 90% initial damage, the total pore area of the three kinds of pores first decreased and then increased with the decrease in temperature for the sample with different low-temperature freezing–thawing–saturation conditions, and the area of micro-pores increased monotonically. The area of meso-pores reduced (25 to -10° C) after an increase ($-10 \text{ to } -20^{\circ}$ C), and the area of macro-pores first decreased (25 to -10° C) and then increased (-10° C to -15° C and $-15 \text{ to } -20^{\circ}$ C).

4 Establishment and validation of microscopic damage model

4.1 Damage model based on pore size distribution

The theory on the origin of damage mechanics was first proposed by Kachanov [70], who proposed the expression

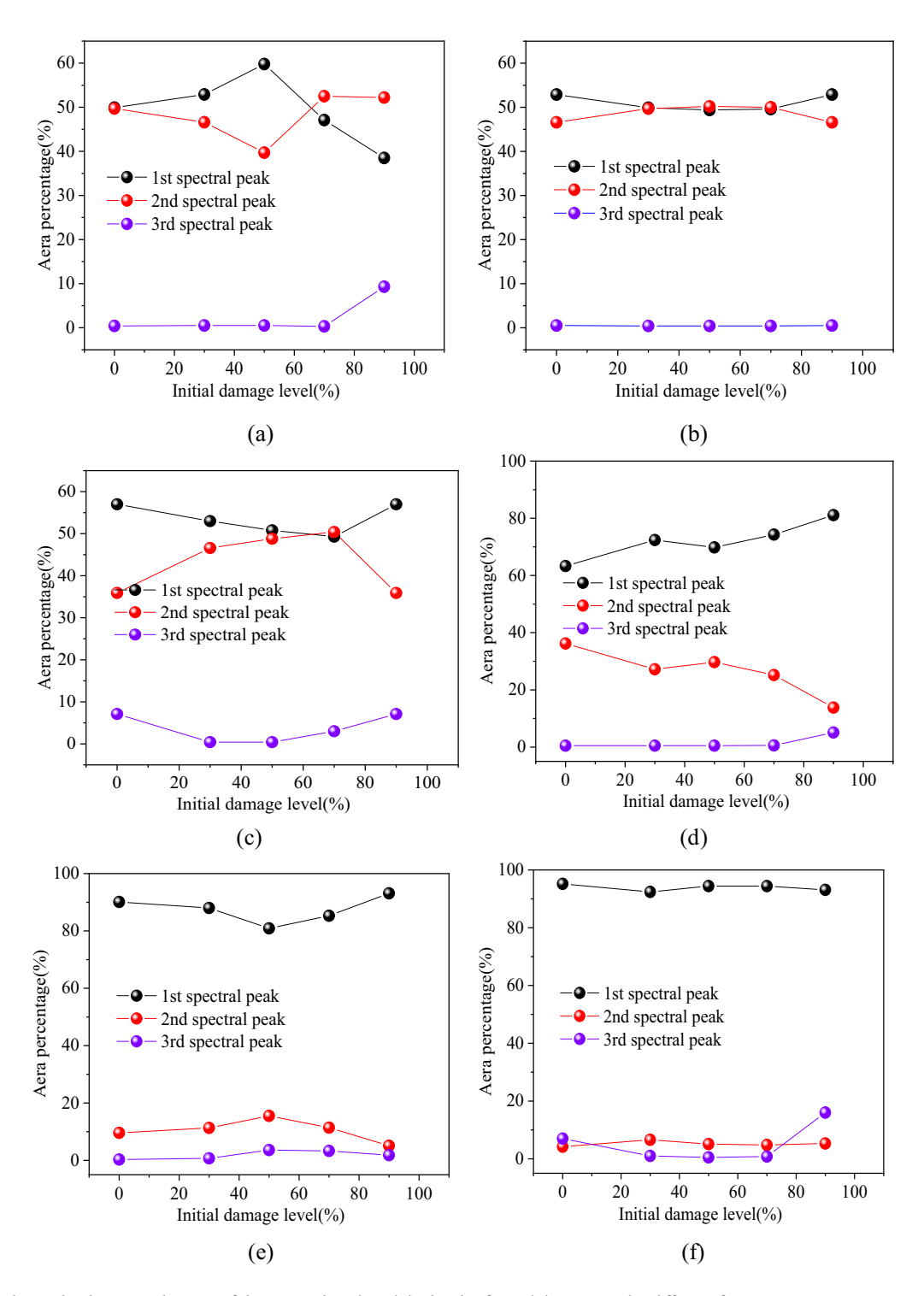


Figure 13: Relationship between the area of the spectral peak and the levels of initial damage under different freezing temperatures: (a) 25° C, (b) 0° C, (c) -5° C, (d) -10° C, (e) -15° C, and (f) -20° C.

for the damage factor that considers the effective load-bearing area:

$$\eta = \frac{C_0}{C},\tag{2}$$

where η is the continuum parameter, C is the initial area, and C_0 is the effective bearing area. On this basis, Rabotnov introduced the damage variable $D_{\rm m}$ [71]:

$$D_{\rm m} = 1 - \eta. \tag{3}$$

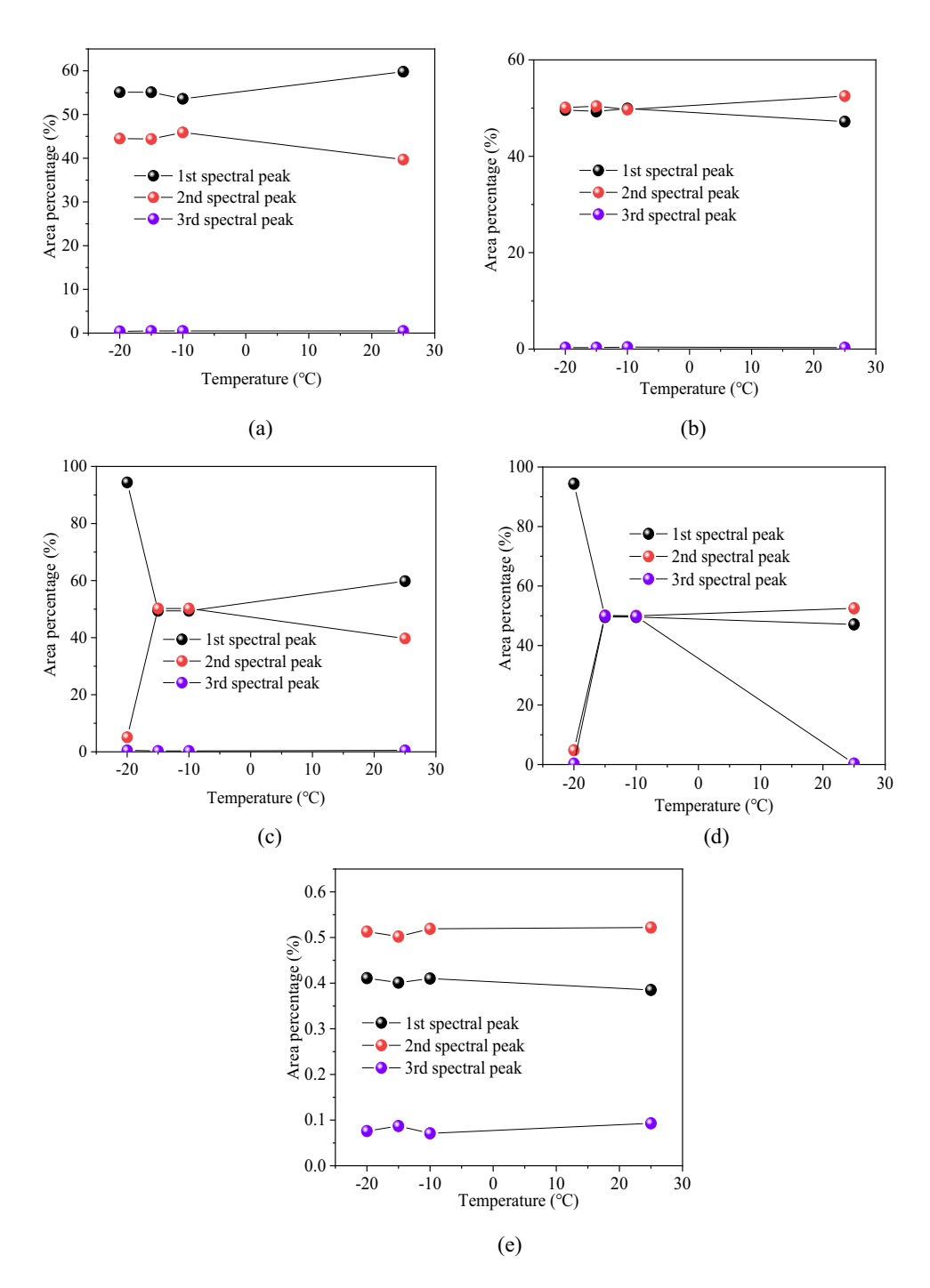


Figure 14: Relationship between the area of spectral peak and the temperature during the process of thawing. (a) 0 UCS (b) 0.3 UCS, (c) 0.5 UCS (d) 0.7 UCS, and (e) 0.9 UCS.

Currently, numerous scholars have established numerous significant damage models for quasi-brittle materials such as rocks based on basic physical and mechanical parameters. There are porosity, static elastic modulus, dynamic-elastic modulus, volume, P-wave, fractal dimension, energy, and so on [72,73]. The pore size distribution has significant effects on rock damage [74]. Therefore, the damage variables were established considering the different pore sizes of the rock

after a subzero freezing–thawing treatment in this study. Different spectral areas represent the pore content of the corresponding size from the T_2 spectrum, then:

$$D_{\rm n} = (P'_{\rm micro}, P'_{\rm meso}, P'_{\rm macto}, P_{\rm micro}, P_{\rm meso}, P_{\rm macro}), \tag{4}$$

where $P_{\rm micro}$, $P_{\rm meso}$, and $P_{\rm macro}$, respectively, represent the spectral areas of micro-pores, meso-pores, and macropores in the T_2 spectrum of the sandstone that is not

exposed to freezing–thawing after NMR testing; $P'_{\rm micro}$, $P'_{\rm meso}$, and $P'_{\rm macro}$, respectively, represent the micro-pores, meso-pores, and macro-pores in the T_2 spectrum after freezing–thawing. The damage variable and the expression of the peak area before and after freezing–thawing are presented as follows:

$$D_{\rm n} = \frac{dP'_{\rm micro} + eP'_{\rm meso} + fP'_{\rm macro}}{dP_{\rm micro} + eP_{\rm meso} + fP_{\rm macro}} - 1,$$
 (5)

where, d, e, and f are, respectively, the weights of micropores, meso-pores, and macro-pores on the damage of the rock.

The coefficient of variation is also known as the dispersion coefficient or standard margin, which is another statistic that measures the variability of observations in data. When comparing two or more degrees of variation, the standard deviation can be used directly if the unit of measure is the same as the mean. If the unit and/or mean are different, the standard deviation should not be used to compare the degree of variation, but the ratio of standard deviation to mean (relative value) should be used for comparison. The ratio of the standard deviation to the mean is called the coefficient of variation and denoted coefficient of variation (CV). The coefficient of variation can eliminate the effect of different units or means on the self-comparison of the degree of variation between two or more data. The standard coefficient of variation is the ratio of the variation index of a group of data to its average index, which is a relative variation index. The coefficient of variation includes full distance coefficient, mean difference coefficient, and standard deviation coefficient. The standard deviation coefficient is commonly used, which is expressed as CV.

The coefficient of variation of the spectral peak area corresponding to the pores of each size inside the sandstone after different freezing—thawing conditions is obtained by the following formula:

$$CV_i = 1 - \frac{\beta_i}{\overline{\theta_i}},\tag{6}$$

where CV_i is the coefficient of variation of the peak area index for the micro-pores, meso-pores, and macro-pores; β_i is the standard deviation of the peak area index for the micro-pores, meso-pores, and macro-pores; $\overline{\theta_i}$ is the average of the peak area index for the micro-pores, meso-pores, and macro-pores.

The coefficient of variation's function is to reflect the degree of dispersion in the unit mean. It is often used to compare the degree of dispersion of two unequal population means. If the mean values of the two populations are equal, the coefficient of the comparative standard deviation is equivalent to the comparative standard deviation.

The coefficients of variation of the peak areas of the micropores, meso-pores, and macro-pores are shown in Table 4. The indicators with a larger coefficient of variation can better reflect the difference in the assessment unit. The corresponding weight is calculated by the following formula:

$$W_i = \frac{C.\ V_i}{\overline{\sum_i C.\ V_i}}.$$
 (7)

The weights *d*, *e*, and *f* of the micro-pores, meso-pores, and macro-pores are presented in Table 5.

If and only if the pore content of the three sizes does not transform before and after the freezing–thawing, the damage variable $D_{\rm n}=0$; it is considered that the freezing–thawing does not cause damage. This model is more applicable than considering only the damage variable of porosity.

It is found from Figure 15 that the curve is concave up by analyzing the relationship between damage variables and freezing—thawing temperature for samples with 90% initial damage. The damage variable $D_{\rm T}$ gradually increased, and the increasing rate dramatically increased as the temperature of freezing—thawing decreased, which was consistent with the variation tendency of porosity. It is discovered by fitting the fact that $D_{\rm T}$ and the freezing—thawing temperature meet the following relationship:

$$\begin{split} k &= 0\%: D_{\mathrm{T}} = 1.5 \times 10^{-4} T^2 - 0.00316 T - 0.0184 \ (R^2 \\ &= 0.9504) \\ k &= 30\%: D_{\mathrm{T}} = 9.4 \times 10^{-5} T^2 - 0.00417 T - 0.0452 \ (R^2 \\ &= 0.9545) \\ k &= 50\%: D_{\mathrm{T}} = 5.3 \times 10^{-5} T^2 - 0.00406 T - 0.06822 \ (R^2 \\ &= 0.98577) \\ k &= 70\%: D_{\mathrm{T}} = 1.07 \times 10^{-4} T^2 - 0.0047 T + 0.005044 T \ (R^2 \\ &= 0.98961) \\ k &= 90\%: D_{\mathrm{T}} = 1.07 \times 10^{-4} T^2 - 0.0047 T + 0.005044 T \ (R^2 \\ &= 1), \end{split}$$

where *k* is the initial damage level and *T* is the freezing–th-awing temperature.

Table 4: Coefficients of variation of the peak areas of micro-pores, meso-pores, and macro-pores

Initial damage level	oucs	0.3UCS	0.5UCS	0.7UCS 0.9UCS
Temperature	Coefficie	ent of varia	ation	
−10°C	0.03236	8255 0.	239921927	2.046902189
−15°C	0.010701	435 0.	246777108	2.141699962
-20°C	0.013285	5804 0.	236166311	2.087928327

Table 5: Weights <i>d</i> , <i>e</i> , and	f of the micro-pores, meso-pores, a	nd macro-pores

Initial damage level	oucs	0.3UCS	0.5UCS	0.7UCS	0.9UCS
Temperature	Weights				
−10°C	d = 0.517	d = 0.247	d = 0.302	d = 0.32	d = 0.142
−15°C	e = 0.102	e = 0.286	e = 0.365	e = 0.3	e = 0.108
-20°C	<i>f</i> = 0.381	<i>f</i> = 0.467	<i>f</i> = 0.333	<i>f</i> = 0.38	<i>f</i> = 0.75

4.2 Damage model verification

In order to explain the damage caused by freezing—thawing, the change of voidage was used for quantitative analysis. It is assumed that the total porosity of the samples changes under the action of freezing—thawing, and the damage of pores of different sizes in the samples is consistent with the variation tendency of the total porosity, indicating that Eq. (5) is applicable. The denominator is constant from the expression of damage factor, and we just need to determine the relationship between the numerator and the total porosity.

Assuming that the total spectral area of the T_2 distribution is S, the following relation is established:

$$P_{\text{micro}} + P_{\text{meso}} + P_{\text{macro}} = S$$

$$dP_{\text{micro}} + eP_{\text{meso}} + fP_{\text{macro}} = F$$

$$d + e + f = 1$$
(8)

Samples are subject to n F-T cycles, and the total area of T_2 spectrum is S' ($S' \ge S$).

$$P'_{\text{micro}} + P'_{\text{meso}} + P'_{\text{macro}} = S'$$

$$dP'_{\text{micro}} + eP'_{\text{meso}} + fP'_{\text{macro}} = F'$$

$$d + e + f = 1$$
(9)

However, in the case that the total porosity of the sample does not alter, the internal pores of the samples

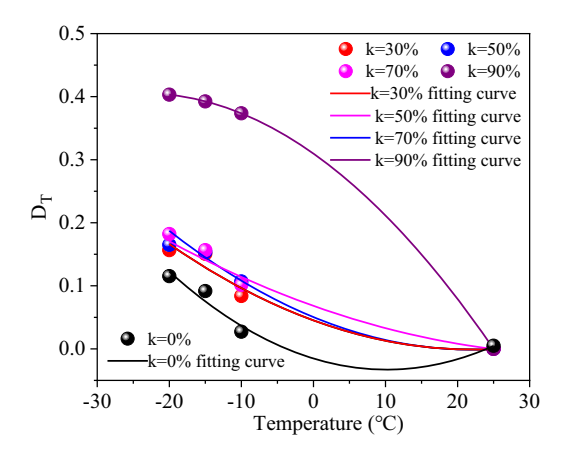


Figure 15: Relationship between damage variables and temperature.

changed, and the sample will also be damaged. Therefore, even if the total porosity of the sample does not transform, it cannot be said that the sample has not been damaged. It is assumed that the total area of T_2 spectra damaged after freezing–thawing is given by S', $dP_{\rm micro} + eP_{\rm meso} + fP_{\rm macro} = S$. The relationship between the damage variable and the three size apertures is presented:

$$D_{\rm n} = \frac{dP'_{\rm micro} + eP'_{\rm meso} + fP'_{\rm macro}}{S} - 1$$

$$P'_{\rm micro} + P'_{\rm meso} + P'_{\rm macro} = S'$$
(10)

The partial derivative of the expression is calculated as:

$$\frac{\partial D_{\rm n}}{\partial P_{\rm micro}} = d/F$$

$$\frac{\partial D_{\rm n}}{\partial P_{\rm meso}} = e/F$$

$$\frac{\partial D_{\rm n}}{\partial P_{\rm macro}} = f/F$$
(11)

which shows that with the increase of the content of the macro-pores, the increase of $D_{\rm n}$ is greater when the total pores remain unaltered. Therefore, the damage model considering the pore content of different sizes is proved to be reasonable again.

4.3 Damage evolution of sandstone after initial damage action

The samples with different initial damage levels have different responses to freezing—thawing treatment under the same loading. In order to study the freezing—thawing damage effect of samples with different levels of initial damage, the relationship between damage factors and the levels of initial damage from preloading is plotted in Figure 16 under different various temperature conditions. The damage factors increased with the increase of the initial damage levels of the samples. The main reason for the degradation of mechanical properties of saturated sandstone samples after freezing—thawing is the water—ice phase transformation in the pores [75—77]. It is remarkable

pointing out that the fitting effect of damage factors is consistent with the change of the initial damage level. It is found through fitting that D_k and the initial damage level satisfy the following relationship:

$$T = -10^{\circ} \text{ C: } D_k = 2 \times 10^{-6} k^3 - 0.0002 k^2 + 0.0077 k$$

$$- 0.0018 (R^2 = 0.9925)$$

$$T = -15^{\circ} \text{ C: } D_k = 2 \times 10^{-6} k^3 - 0.0003 k^2 + 0.0111 k$$

$$- 0.0004 (R^2 = 0.9995)$$

$$T = -20^{\circ} \text{ C: } D_k = 2 \times 10^{-6} k^3 - 0.0002 k^2 + 0.0106 k (R^2 = 1).$$

All of them accord with the polynomial function relation and have a good fitting effect. The results can be used to quantitatively evaluate the damage of the samples treated by low-temperature freezing-thawing and different levels of initial damage from preloading.

Discussion

DE GRUYTER

5.1 Damage parameter based on the NMR porosity

Porosity is an effective parameter to evaluate the degree of damage to rock. Therefore, the damage variable D_p was introduced into the porosity of different initial damage levels, as follows:

$$D_{\rm P} = \frac{P_{\rm i} - P_{\rm 0}}{P_{\rm f} - P_{\rm 0}},\tag{12}$$

where $P_{\rm f}$ is the porosity with an initial damage of 100%, $P_{\rm 0}$ is the initial porosity before pre-loading, and P_i is the porosity with a certain initial damage after preloading.

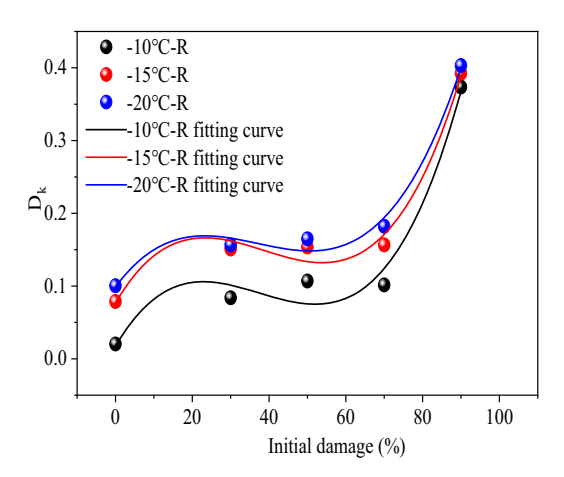


Figure 16: Relationship between damage variables and the levels of initial damage.

The damage variables obtained by the changes of porosity after different initial damage levels can reflect the overall degradation characteristics of the sample at a certain loading level. Figure 17 shows the fitting curve of porosity change with initial damage from preloading. It can be found from Figure 17 that the fitting curve has a good correlation with the sample porosity in the range of 0-90% UCS. When the preloading damage level reached 100%, that is, when the loading ratio reached 1, it can be predicted that the porosity of the sample is 5.23079% according to the above fitting curve of porosity and the loading ratio. By substituting Eq. (12) into the linear fitting equation, the relationship between damage parameters and loading stress ratio can be written as follows:

$$D_{\rm p} = 0.971k + 0.029. \tag{13}$$

The porosity and degradation evolution at different specific loading stages can also be deduced in the same way. In addition, the results of this study were highly consistent with those of previous studies [78-82].

5.2 Mechanism analysis of rock freezing-thawing failure process

Water, ice, rock, and other multi-phase media in rock mass have different thermo-physical properties, and the change of their thermo-physical properties is the essence of rock freezing-thawing damage. As the temperature decreased, different mineral grain sizes shrunk inside the rocks, while pore water containing mineral grains froze into ice and expanded. Due to the different expansion rates and thermo-elastic properties of the crystal orientation of various mineral particles, there is uncoordinated shrinkage and expansion at the boundary of the particles, generating local tensile and compressive stresses

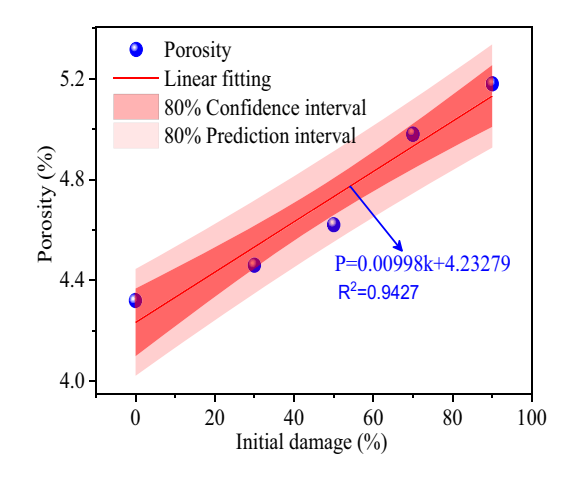


Figure 17: Variations of the porosity against the initial damage.

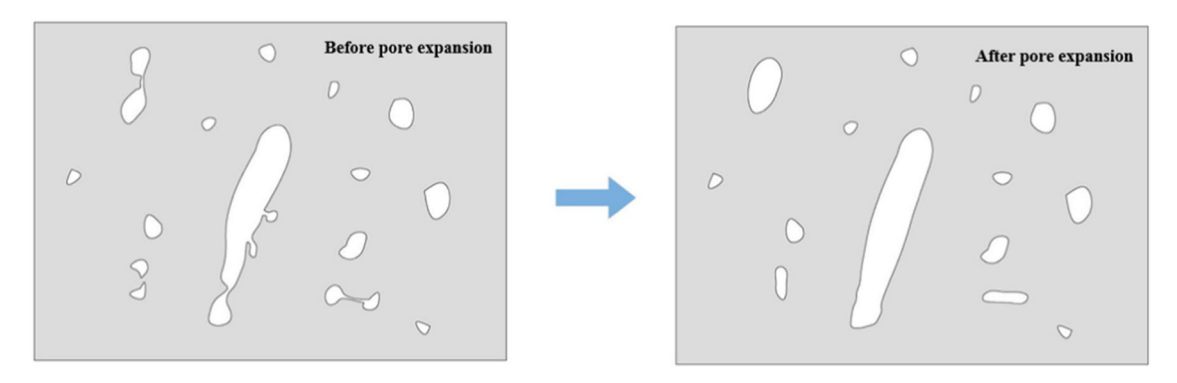


Figure 18: Schematic diagram of micro-pores penetrating meso-pores and macro-pores [59].

(frost-heaving stress) between the mineral particles and micro-pores to limit the expansion. This internal stress is destructive to some rock particles with weak cementation strength, causing local damage inside the rock. When the temperature was increased, pore water in mineral grains gradually thawed and migrated, and frost-heaving stress was released, causing mineral particles to fall off and compaction degree decrease, thereby resulting in micro-pores gradually penetrating meso-pores and macro-pores (Figure 18).

Perforated channels form between micro-pores, meso-pores, and macro-pores, leading to a loss of mineral particles that fell off after thawing (Figure 19). Further destruction and accumulation of pores led to the development of original pores and the generation of new fractures, while the concentration of frost-heave at the end of pores led to the concentration of stress at the crack tip, leading to the further development of fractures. As the temperature was increased again, pore ice transformed into liquid water again, and the original pores and new cracks became new channels for pore water to transport, making frost-heaving occur again in the next freezing process. The

lithology became more and more softer, and the degree of damage deterioration gradually increased with the increase of saturation, leading to a series of physical and mechanical alternation changes, such as shrinkage, expansion, damage, and cracking. The decrease of the strength and elastic modulus of rock samples reflected the deterioration of the internal structure under the conditions of freezing—thawing and loading.

5.3 Damage evolution equation of rock under freezing-thawing and loading

UCS tests at a 0.5 MPa·min⁻¹ loading rate were performed on the samples with the level of initial damage that had been exposed to different subzero temperature freezing and thawing (0, -5, -10, -15, and -20°C). Figure 20 shows the stress–strain curves of samples with different initial damage levels of 0, 30, 50, 70, and 90%. For the stress–strain curve of the samples without initial damage after

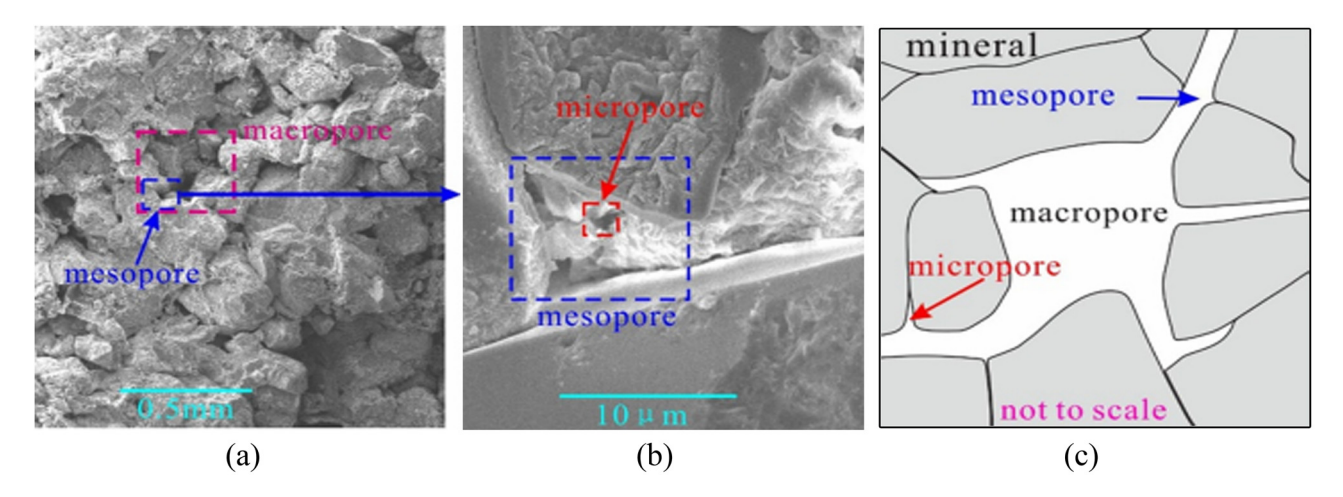


Figure 19: Pore structure of sandstone observed via scanning electron microscopy [60]: (a) 25 times, (b) 1,000 times, and (c) pore structure model.

DE GRUYTER

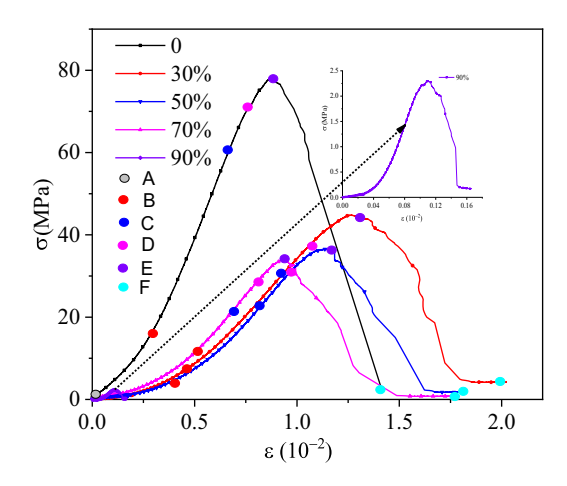


Figure 20: Stress–strain curves of sandstone samples after low-temperature freezing–thawing at initial damage levels of 0, 30, 50, 70, and 90%.

subzero treatment, it can be roughly divided into five stages: the crack closure stage (AB), elastic stage (BC), stable cracking stage (CD), unstable cracking stage (DE), and post-peak stage (EF) [59].

According to the theory of damage mechanics, the macroscopic physical properties of rock can represent the degree of deterioration inside the rock material. Because the elastic modulus of rock material after freezing—thawing is easy to analyze and measure, the elastic modulus can be used as a significant parameter to evaluate rock damage [83]. The rock damage variable after a subzero freezing—thawing treatment can be defined as

$$D_{\rm C} = 1 - \frac{E_{\rm T}}{E_{\rm O}},\tag{14}$$

where $E_{\rm T}$ is elastic modulus after a subzero freezing–thawing treatment. The relationship between damage variables

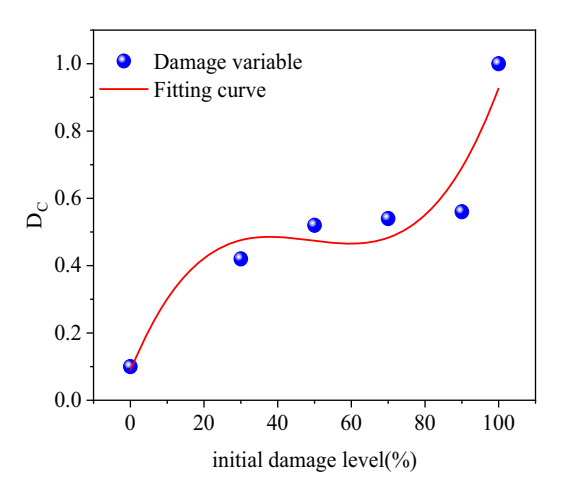


Figure 21: Relationship between damage variables and initial damage.

calculated by the elastic modulus and initial damage is shown in Figure 21.

The analysis and research results from microscopic and macroscopic points of view show that there are certain differences in the internal damage behavior of rocks. There are obvious differences between the damage variables of rock obtained by NMR theory and classical mechanics theory, indicating that the damage degree measured by the NMR method was lower than that by classical rock mechanics theory. The reason for the difference is that the interaction between the micro-pores, meso-pores, and macro-pores is ignored in the damage model only considering the micro-pores, meso-pores, and macro-pores by NMR theory.

In fact, the internal stress acts on the skeleton of rock mass in a cyclic and alternating manner with the external temperature, which leads to an irreversible deterioration of physical and mechanical properties of rock mass with the decrease in freezing—thawing temperature gradient.

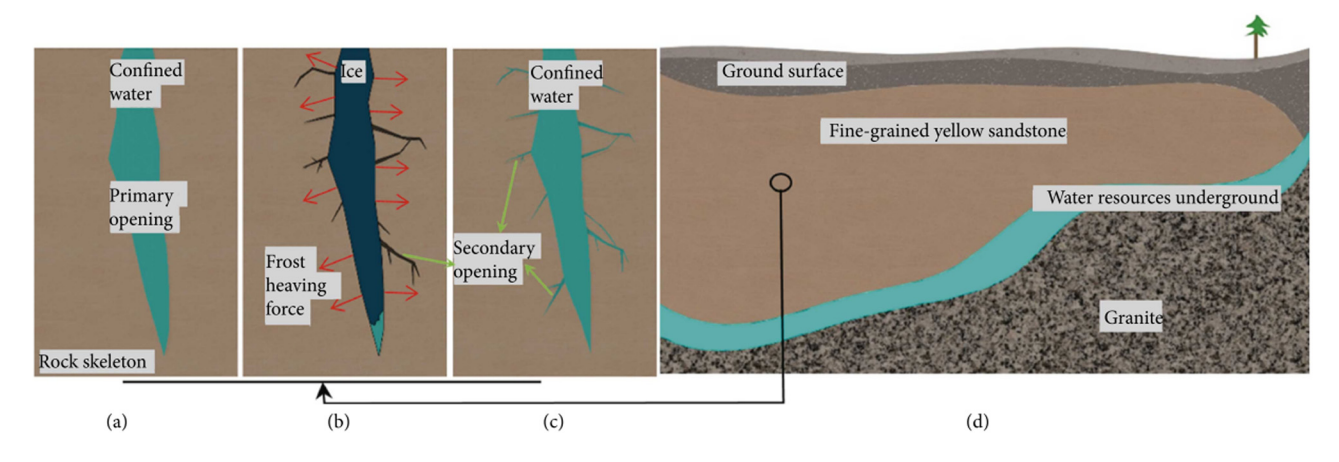


Figure 22: Schematic diagram of freeze-thaw damage [84].

The action of external loading caused further slippage and dislocation of mineral particles inside the rock, a large number of micro-cracks initiating, expanding, and nucleating, the local damage domain gradually connecting, finally coalescing and forming macro-cracks, which aggravate the damage and fracture process of rock (Figure 22). Therefore, the freezing-thawing damage process of the rock mass is a fatigue damage process. The freezing-thawing damage makes the internal structure of the rock and the basic mechanical properties present different degrees of attenuation trend, which is bound to cause the decline of rock-bearing capacity. However, when the damage degree is the same, the strain increases with the increase of the number of freezingthawing cycles, and the plastic deformation of the rock is particularly obvious, presenting the characteristics of ductile failure at the late stage of deformation.

In this study, samples with different initial degrees of damage were subjected to alternating freezing-thawingsaturation action under different temperature gradients, resulting in numerous new micro-cracks formation, the gradual expansion and coalescence of the existing cracks, and finally the formation of macroscopic cracks in the rock mass. Thus, microscopic and macroscopic damage occurred in the samples. However, the NMR can only measure the area of the micro-pores, meso-pores, and macro-pores by measuring the content of water in the pores, and the macroscopic crack area cannot be measured as water flows out of the macroscopic crack. Therefore, the degree of damage measured only by the NMR method is lower than that by classical rock mechanics theory. Thus, only by considering the micro-pores, the meso-pores, and the macro-pores from the microscopic perspective, the established damage model cannot more precisely and effectively evaluate the real damage state inside the rock, which requires further investigation in the future.

6 Conclusions

In this article, various levels of initial damage were fabricated by previous loading and unloading tests, and the pore structures of sandstone samples with various levels of initial damage were measured using the NMR technique under five subzero-temperature freezing—thawing processes. The main conclusions can be summarized as follows:

As the initial damage level increased, the P-wave velocity of the sample decreased, while the porosity increased, which proved that initial damage is indeed generated by uniaxial loading and unloading of the sample. In addition, the changes of P-wave velocity and porosity were in good

agreement, both of which indicating the accumulation of damage and material deterioration as the initial damage level was increased.

The peak signal intensity of the micro-pores, mesopores, and macro-pores decreased as the temperature declined. The peak signal intensity of the micro-pores, the meso-pores were significant obvious declining as the initial damage degree increasing at subzero temperature conditions.

The distribution of T₂ signal intensity exposed to the low-temperature freezing-thawing-saturation treatment was rather larger than that under normal temperature conditions for samples with different initial damage levels, indicating that the low-temperature freezing-thawing condition would promote the porosity and degree of damage increase for samples with different initial damage levels.

The larger the levels of initial damage, the larger the T2 peak value obtained after freezing—thawing—saturation treatment at a low temperature. The change of meso-pores was mainly divided into two obvious growth stages, the levels of initial damage were from 0 to 70% and from 70 to 90%, and the peak value of meso-pores increased rapidly.

The low temperature would also cause the free water to freeze—thaw repeatedly for the sample with different levels of initial damage, causing the pore size to expand and extend; new micro-pores would continue to develop, and the micro-pores connected to form macro-pores, showing that the total pores increased gradually.

A continuum damage model considering freezing—thawing damage from different pore sizes was finally introduced to describe the damage evolution of the samples with different levels of initial damage under super-zero temperature freezing—thawing—saturation conditions. The results can be used to quantitatively evaluate the damage of sandstone samples with different initial damage degrees under the low-temperature freezing—thawing treatment.

Furthermore, the analysis and research results from microscopic and macroscopic points of view show that there were obvious difference between the damage variables of rock obtained by NMR theory and classical mechanics theory, and the degree of damage measured by the NMR method was lower than that by classical rock mechanics theory.

Funding information: This research was supported by National Natural Science Foundation of China (Grant Nos 52274118 and 52274194), the Key project of Hunan Provincial Education Department (22A0337), and Hunan Provincial Natural Science Found of China (2023][50232).

Author contributions: Shuailong Lian: writing – original draft and visualization. Wen Wan: investigation,

conceptualization, and methodology. Yanlin Zhao: writing – review and editing. Wenging Peng: validation. Can Du: formal analysis. Hao Hu: software and data curation. All authors reviewed the manuscript. All authors have accepted responsibility for the entire content of this manuscript and approved its submission.

Conflict of interest: The authors state no conflict of interest.

References

- Yang, Z. D., X. D. Ma, L. W. Xu, S. J. Hou, D. Z. Ren, and Q. Feng. A new analytical solution on the frost heaving force of circular tunnel in cold regions. Rock Mechanics and Rock Engineering, Vol. 57, 2024, pp. 3483-3508.
- [2] Zhao, Y. L., Y. X. Wang, W. J. Wang, L. M. Tang, and Q. Liu. Modeling of rheological fracture behavior of rock cracks subjected to hydraulic pressure and far field stresses. Theoretical and Applied Fracture Mechanics, Vol. 101, 2019, pp. 59-66.
- Zhao, Y. L., L. Y. Zhang, W. J. Wang, W. Wan, and W. H. Ma. Separation of elastoviscoplastic strains of rock and a nonlinear creep model. International Journal of Geomechanics, Vol. 18, 2018, id. 04017129.
- [4] Zhou, Z. Q., J. Bi, Y. Zhao, C. L. Wang, and Y. F. Zhang. Thermalmechanical coupling smooth particle hydrodynamics-phase field method modelling of cracking in rocks. Computers and Geotechnics, Vol. 173, 2024, id. 106476.
- Liu, Q. S., Z. C. Qian, and Z. J. Wu. Micro/macro physical and mechanical variation of red sandstone subjected to cyclic heating and cooling: an experimental study. Bulletin of Engineering Geology and the Environment, Vol. 78, No. 3, 2017, pp. 1485-1499.
- Niu, Y., X. P. Zhou, J. Z. Zhang, and Q. H. Qian. Experimental study on crack coalescence behavior of double unparallel fissure-contained sandstone specimens subjected to freeze-thaw cycles under uniaxial compression. Cold Regions Science and Technology, Vol. 158, 2019, pp. 166-181.
- [7] Zhao, Y. L., Y. X. Wang, W. J. Wang, W. Wan, and J. Z. Tang. Modeling of non-linear rheological behavior of hard rock using triaxial rheological experiment. International Journal of Rock Mechanics and Mining Sciences, Vol. 93, 2017, pp. 66-75.
- Wang, M., W. Wan, and Y. L. Zhao. Experimental study on crack propagation and coalescence of rock-like materials with two preexisting fissures under biaxial compression. Bulletin of Engineering Geology and the Environment, Vol. 79, No. 6, 2020, pp. 3121-3144.
- Zhao, Y., P. F. He, Y. F. Zhang, and C. L. Wang. A new criterion for a toughness-dominated hydraulic fracture crossing a natural frictional interface. Rock Mechanics and Rock Engineering, Vol. 52, 2019, pp. 2617-2629.
- [10] Wang, M., Z. X. Lu, Y. L. Zhao, and W. Wan. Experimental and numerical study on peak strength, coalescence and failure of rocklike materials with two folded preexisting fissures. Theoretical and Applied Fracture Mechanics, Vol. 125, 2023, id. 103830.
- [11] Qi, J. J., Y. N. Ye, Z. Huang, W. R. Lv, W. B. Zhou, F. C. Liu, et al. Experimental study and theoretical analysis of steel-concrete composite box girder bending moment-curvature restoring force. Sustainability, Vol. 15, No. 8, 2023, id. 6585.

- [12] Wang, M., Z. X. Lu, Y. L. Zhao, and W. Wan. Peak strength, coalescence and failure processes of rock-like materials containing preexisting joints and circular holes under uniaxial compression: Experimental and numerical study. Theoretical and Applied Fracture Mechanics, Vol. 125, 2023, id. 103898.
- Huang, S. B., Q. S. Liu, Y. Z. Liu, Y. S. Kang, A. P. Cheng, and Z. Y. Ye. Frost heaving and frost cracking of elliptical cavities (fractures) in lowpermeability rock. Engineering Geology, Vol. 234, 2018, pp. 1-10.
- Li, J., K. Zhou, W. Liu, and Y. Zhang. Analysis of the effect of free-[14] ze-thaw cycles on the degradation of mechanical parameters and slope stability. Bulletin of Engineering Geology and the Environment, Vol. 77, No. 2, 2018b, pp. 57-580.
- [15] Huang, S. B., Y. B. He, G. F. Liu, Z. X. Lu, and Z. K. Xin. Effect of water content on the mechanical properties and deformation characteristics of the clay-bearing red sandstone. Bulletin of Engineering Geology and the Environment, Vol., 80, 2020, pp. 1767-1790.
- Zhao, Y. L., S. L. Luo, Y. X. Wang, W. J. Wang, L. Y. Zhang, and W. Wan. Numerical analysis of karst water inrush and a criterion for establishing the width of water-resistant rock pillars. Mine Water and the Environment, Vol. 36, No. 4, 2017, pp. 508-519.
- Wu, Q. H., Y. Yang, K. X. Zhang, Q. Y. Li, W. Chen, and Z. F. Liu. Study on the mechanical properties and deterioration mechanism of sandstones under different humidity conditions. Journal of Central South University, Vol. 30, No. 12, 2023, pp. 4252-4267.
- Chen, W., W. Wan, Y. L. Zhao, and W. Q. Peng. Experimental study of the crack predominance of rock-like material containing parallel double fissures under uniaxial compression. Sustainability, Vol. 12, No. 12, 2020, id. 5188.
- [19] Li, T. Y., Y. Zhao, and J. Liao. Experimental study on the seepage characteristics of dolomite fracture specimens before and after grouting. Archive of Applied Mechanics, Vol. 94, 2024, pp. 1723-1738.
- Zhang, J. F., S. L. Shi, Y. Lu, B. You, F. H. Wu, L. Z. Zhang, et al. Coal mine gas abnormal emission inducing factors, manifestation emission mechanism. Fresenius Environmental Bulletin, Vol. 31, 2022, pp. 6569-6575.
- [21] Zheng, K., C. L. Wang, Y. Zhao, J. Bi, and H. F. Liu. A modified threedimensional mean strain energy density criterion for predicting shale mixed-mode I/III fracture toughness. Journal of Rock Mechanics and Geotechnical Engineering, Vol. 16, 2024, pp. 1–18.
- [22] Lu, Y., H. Li, J. X. Lu, S. L. Shi, G. Wang, Q. Ye, et al. Clean up water blocking damage in coalbed methane reservoirs by microwave heating: laboratory studies. Process Safety and Environmental Protection, Vol. 138, 2020, pp. 292-299.
- [23] Weng, L., Z. Wu, Q. Liu, Z. Chu, and S. Zhang. Evolutions of the unfrozen water content of saturated sandstones during freezing process and the freeze-induced damage characteristics. International Journal of Rock Mechanics and Mining Sciences, Vol. 142, 2021, id. 104757.
- [24] Huang, S. B., Y. H. Ye, X. Z. Cui, A. P. Cheng, and G. F. Liu. Theoretical and experimental study of the frost heaving characteristics of the saturated sandstone under low temperature. Cold Regions Science and Technology, Vol. 174, 2020, id. 103036.
- Yu, W. J., K. Li, Z. Liu, B. F. An, P. Wang, and H. Wu. Mechanical characteristics and deformation control of surrounding rock in weakly cemented siltstone. Environmental Earth Science, Vol. 80, No. 9, 2021, id. 337.
- Wu, Q. H., C. L. Xie, Y. S. Xie, Y. L. Zhao, X. F. Li, J. Liu, et al. Extending application of asymmetric semi-circular bend specimen to investigate mixed mode I/II fracture behavior of granite. Journal of Central South University, Vol. 29, No. 4, 2022, pp. 1289-1304.

- [27] Pang, J. W., X. J. Yang, S. Q. Yang, Y. L. He, J. L. Xie, and Q. Y. Han. A method for dividing rockburst risk zones – A case study of the hegang mining area in China. Sustainability, Vol. 15, 2023, id. 9568.
- [28] Huang, S. B., Y. Z. Liu, Y. L. Guo, Z. Zhang, and Y. Cai. Strength and failure characteristics of rock-like material containing single crack under freeze-thaw and uniaxial compression. *Cold Regions Science* and Technology, Vol. 162, 2019, pp. 1–10.
- [29] Yuan, Z. G., J. T. Zhao, S. Q. Li, Z. H. Jiang, F. Huang, A unified solution for surrounding rock of roadway considering seepage, dilatancy, strain-softening and intermediate principal stress. *Sustainability*, Vol. 14, No. 13, 2022, id. 8099.
- [30] Zhai, C., L. Qin, S. Liu, J. Xu, Z. Tang, and S. Wu. Pore structure in coal: pore evolution after cryogenic freezing with cyclic liquid nitrogen injection and its implication on coalbed methane extraction. *Energ and Fuel*, Vol. 30, No. 7, 2016, pp. 6009–6020.
- [31] Huang, S. B., Z. X. Lu, Z. Y. Ye, and Z. K. Xin. An elastoplastic model of frost deformation for the porous rock under freeze-thaw. *Engineering Geology*, Vol. 278, 2020, id. 105820.
- [32] You, B., X. Y. Liang, and K. Q. Liang. Study on non-coal mine wastewater treatment based on response surface methodology (Rsm). Fresenius Environmental Bulletin, Vol. 28, 2019, id. 6264.
- [33] Jia, Z. Z., F. Tao, and Q. Ye. Experimental research on coal-gas outburst prevention by injection liquid freezing during uncovering coal seam in rock crosscut. Sustainability, Vol. 15, No. 3, 2023, id. 1788.
- [34] Ye, Z. Y., L. L. Zhang, Z. H. Zhou, K. Pan, X. B. Liu, W. H. Liu, et al. Mechanical properties of the combination of surrounding rock and primary support under impacting load. *Sustainability*, Vol. 15, No. 5, 2023, id. 6585.
- [35] Zhao, Y. L., Q. Liu, H. Lin, Y. X. Wang, W. Y. Tang, J. Liao, et al. A review of hydromechanical coupling tests, theoretical and numerical analyses in rock materials. *Water*, Vol. 15, No. 13, 2023, id. 0239.
- [36] Huang, S. B., Z. K. Xin, Y. H. Ye, and F. Liu. Study on the freeze–thaw deformation behavior of the brittle porous materials in the elastoplastic regime based on Mohr-Coulomb yield criterion. *Construction and Building Materials*, Vol. 268, 2021, id. 121799.
- [37] He, Y. C. and Q. N. Chen. Construction and application of LSTM-based Prediction model for tunnel surrounding rock deformation. Sustainability, Vol. 15, No. 8, 2023, id. 6877.
- [38] Yan, T., C. Q. Zhu, Q. F. Li, and Q. Xu. Investigating disaster mechanisms triggered by abrupt overburden fracture alterations in close-seam mining beneath an exceptionally thick sandstone aquifer. Sustainability, Vol. 15, No. 18, 2023, id. 13845.
- [39] Du, C., J. Bi, Y. Zhao, C. Wang, W. Tang, and S. Lian. Investigation of pore structure evolution and damage characteristics of high temperature rocks subjected to liquid nitrogen cooling shock. *International Journal of Damage Mechanics*, 2024, pp. 1–35.
- [40] Yu, W. J., H. X. Guo, K. Li, and B. Pan. Experimental Study on uniaxial compression mechanics and failure characteristics of non-through fractured rock. *Sustainability*, Vol. 15, No. 6, 2023, id. 4968.
- [41] Huang, S. B., Q. S. Liu, A. P. Cheng, and Y. Z. Liu. A statistical damage constitutive model under freeze-thaw and loading for rock and its engineering application. *Cold Regions Science and Technology*, Vol. 145, 2018, pp. 142–150.
- [42] Qin, L., C. Zhai, S. Liu, J. Xu, S. Wu, and R. Dong. Fractal dimensions of low rank coal subjected to liquid nitrogen freeze-thaw based on nuclear magnetic resonance applied for coalbed methane recovery. *Powder Technology*, Vol. 325, 2018, pp. 11–20.
- [43] Li, Y. H., X. Zeng, Z. Lin, J. Su, T. Gao, R. J. Deng, et al. Experimental study on phosphate rock modified soil-bentonite as a cut-off wall material. *Water Supply*, Vol. 22, No. 2, 2022, pp. 1676–1690.

- [44] Yang, X., L. Weng, and Z. Hu. Damage evolution of rocks under triaxial compressions: an NMR investigation. *KSCE Journal of Civil Engineering*, Vol. 22, No. 8, 2018, pp. 2856–2863.
- [45] Wang, C. L., L. H. Pan, Y. Zhao, Y. F. Zhang, and W. K. Shen. Analysis of the pressure-pulse propagation in rock: a new approach to simultaneously determine permeability, porosity, and adsorption capacity. *Rock Mechanics and Rock Engineering*, Vol. 52, 2019, pp. 4301–4317.
- [46] You, B., J. X. Xu, S. L. Shi, H. Q. Liu, Y. Lu, and X. Y. Liang. Treatment of Coal Mine Sewage by Catalytic Supercritical Water Oxidation. Fresenius Environmental Bulletin, Vol. 29, 2020, pp. 497–502.
- [47] Wang, P. F., X. H. Tan, L. Y. Zhang, Y. J. Li, and R. Liu. Influence of particle diameter on the wettability of coal dust and the dust suppression efficiency via spraying. *Process Safety Environmental Protection*. Vol. 132, 2019. pp. 189–199.
- [48] Li, J., R. B. Kaunda, and K. Zhou. Experimental investigations on the effects of ambient freeze-thaw cycling on dynamic properties and rock pore structure deterioration of sandstone. *Cold Regions Science* and Technology, Vol. 154, 2018, pp. 133–141.
- [49] Wu, H., Q. Jia, W. J. Wang, N. Zhang, and Y. M. Zhao. Experimental test on nonuniform deformation in the tilted strata of a deep coal mine. *Sustainability*, Vol. 23, 2021, id. 13280.
- [50] Li, M., H. Lv, Y. Lu, D. M. Wang, S. L. Shi, and R. Q. Li. Instantaneous Discharge Characteristics and Its Methane Ignition Mechanism of Coal Mine Rock Damage. *Environmental Science and Pollution Research International*, Vol. 29, No. 41, 2022, pp. 62495–62506.
- [51] Tian, Z. J., Z. Z. Zhang, M. Deng, S. Yan, and J. B. Bai. Gob-side entry retained with soft roof, floor, and seam in thin coal seams: A case study. *Environmental Science Pollution Reports*, Vol. 29, 2021, pp. 16113–16122.
- [52] Sun, Q., Z. Dong, and H. Jia. Decay of sandstone subjected to a combined action of repeated freezing–thawing and salt crystallization. *Bulletin of Engineering Geology and the Environment*, Vol. 78, No. 8, 2019, pp. 5951–5964.
- [53] Dai, S. X., Y. F. Gong, F. Wang, and P. Hu. Diagenesis Evolution of tight sandstones in chang 8 member of upper triassic in the Xiasiwan Area, Ordos Basin, China. *Fresenius Environmental Bulletin*, Vol. 28, No. 8, 2019, pp. 6275–6281.
- [54] Lu, Y., Y. L. Liu, S. L. Shi, G. X. Wang, H. Li, and T. Wang. Micro-particles stabilized aqueous foam for coal spontaneous combustion control and its flow characteristics. *Process Safety Environmental Protection*, Vol. 139, 2020, pp. 262–272.
- [55] Zhao, Y., Y. F. Zhang, C. L. Wang, and Q. Liu. Hydraulic fracturing characteristics and evaluation of fracturing effectiveness under different anisotropic angles and injection rates: An experimental investigation in absence of confining pressure. *Journal of Natural Gas Science and Engineering*, Vol. 97, 2022, id. 104343.
- [56] Qin, B. T., L. Li, D. Ma, Y. Lu, X. X. Zhong, and Y. W. Jia. Control technology for the avoidance of the simultaneous occurrence of a methane explosion and spontaneous coal combustion in a coal mine: A case study. *Process Safety Environmental Protection*, Vol. 103, 2016, pp. 203–211.
- [57] Zhao, Y. L., J. H. Liu, C. S. Zhang, H. Q. Zhang, J. Liao, S. T. Zhu, et al. Mechanical behavior of sandstone during post-peak cyclic loading and unloading under hydromechanical coupling. *International Journal of Mining Science and Technology*, Vol. 33, No. 8, 2023, pp. 927–947.
- [58] Wang, X., B. Z. Ren, Y. Y. Zhou, and X. Y. Shi. Study on the mechanism and kinetics of manganese release from waste manganese ore waste rock under rainfall leaching. *Environmental Science and Pollution Research*, Vol. 29, No. 4, 2022, pp. 5541–5551.

- [59] Liu, T., C. Zhang, J. Li, K. Zhou, and C. Ping. Detecting freeze-thaw damage degradation of sandstone with initial damage using NMR technology. Bulletin of Engineering Geology and the Environment, Vol. 80, 2021, pp. 4529-4545.
- [60] Wang, T., Q. Sun, H. Jia, J. Ren, and T. Luo. Linking the mechanical properties of frozen sandstone to phase composition of pore water measured by LF-NMR at subzero temperatures. Bulletin of Engineering Geology and the Environment, Vol. 80, 2021, pp. 4501-4513.
- [61] Zhang, Y., B. Z. Ren, A. Hursthouse, R. J. Deng, and B. L. Hou. Leaching and releasing characteristics and regularities of sb and as from antimony mining waste rocks. Polish Journal of Environmental Studies, Vol. 28, 2019, pp. 4017-4025.
- [62] Weng, L., Z. Wu, and Q. Liu. Evaluating damage and microcracking behavior of granite using NMR testing under different levels of unconfined compression. *International Journal of Geomechanics*, Vol. 19, No. 1, 2019, id. 04018186.
- [63] Huang, Z. H., L. H. Zhang, Z. J. Yang, J. Zhang, Y. K. Gao, and Y. H. Zhang. Preparation and properties of a rock dust suppressant for a copper mine. Atmospheric Pollution Research, Vol. 10, 2019, pp. 2010-2017.
- [64] Huang, S. B., Q. S. Liu, Y. Z. Liu, Z. Y. Ye, and A. P. Cheng. Freezing strain model for estimating the unfrozen water content of saturated rock under low temperature. International Journal of Geomechanics, Vol. 18, 2018, id. 04017137.
- [65] Pang, J. W., J. L. Xie, Y. L. He, Q. Y. Han, and Y. J. Hao. Study on the distribution trend of rockburst and ground stress in the hegang mining area. Sustainability, Vol. 15, No. 12, 2023, id. 9445.
- [66] Martin, C. D. and N. A. Chandler. The progressive fracture of Lac Du Bonnet granite. International Journal of Rock Mechanics and Mining Sciences and Geomechanics Abstracts, Vol. 31, No. 6, 1994, pp. 643-659.
- [67] Cowan, B. P. Nuclear Magnetic Resonance and Relaxation, Cambridge University Press, Cambridge, 1997, pp. 21-22.
- [68] Dastidar, R. Nuclear Magnetic Resonance (NMR) Study of Freezing and Thawing of Saturated Porous Media and Application to Shale and Pore Volume Compressibility Estimation, University of Oklahoma, Norman, 2007. (Doctoral dissertation).
- [69] Jia, H. L., S. Ding, F. Zi, Y. H. Deng, and Y. J. Shen. Evolution in sandstone pore structures with freeze-thaw cycling and interpretation of damage mechanisms in saturated porous rocks. Catena, Vol. 195, 2020, id. 104915. ISSN 0341-8162.
- [70] Kachanov, L. M. On the creep fracture time. tekhnicheskich nauk, Vol. 8, 1958, pp. 26-31.
- [71] Rabotnov, Y. N. On the equations of state for creep, in progress in applied mechanics. Prager Anniversary Volume, In: W. T. Koiter, (ed), McMillan, New York, 1963, pp. 307-315.
- [72] Zhao, Y., C. L. Wang, and J. Bi. Analysis of fractured rock permeability evolution under unloading conditions by the model of

- elastoplastic contact between rough surfaces. Rock Mechanics and Rock Engineering, Vol. 53, 2020, pp. 5795-5808.
- Wang, B., F. Wang, and Q. Wang. Damage constitutive models of concrete under the coupling action of freeze-thaw cycles and load based on Lemaitre assumption. Construction and Building Materials, Vol. 173, 2018, pp. 332-341.
- Meng, F. D., Y. Zhai, Y. B. Li, R. F. Zhao, Y. Li, and H. Gao. Research on the effect of pore characteristics on the compressive properties of sandstone after freezing and thawing. Engineering Geology, Vol. 286, 2021, id. 106088.
- [75] Cases, J. M., I. Berend, G. Besson, M. Francois, J. P. Uriot, F. Thomas, et al. Mechanism of adsorption and desorption of water vapor by homoionicmontmorillonite. 1. The sodium-exchanged form. Lanamuir, Vol. 8, 1992, pp. 2730-2739.
- [76] Cheng, K. and Z. Heidari. Combined interpretation of NMR and TGA measurements to quantify the impact of relative humidity on hydration of clay minerals. Applied Clay Science, Vol. 143, 2017, pp. 362-371.
- Weng, L., Z. Wu, Q. Liu, and Z. Wang. Energy dissipation and dynamic fragmentation of dry and water-saturated siltstones under sub-zero temperatures. Engineering Fracture Mechanics, Vol. 220, 2019, id. 106659.
- Zhang, J. F., F. F. Yang, R. G. Zhang, J. Y. He, Y. D. Xie, Z. Q. Miao, [78] et al. Experimental research on coal seam structure and gas occurrence influencing factors in Weijiadi Mine China. Fresenius Environmental Bulletin, Vol. 31, 2022, pp. 74-80.
- [79] Lian, S. L., W. Wan, Y. L. Zhao, Q. H. Wu, and C. Du. Investigation of the mechanical behavior of rock-like material with two flaws subjected to biaxial compression. Scientific Reports, Vol. 14, 2024,
- [80] Jia, X. L., J. K. Wu, C. J. Lian, J. J. Wang,, J. L. Rao, R. J. Feng, et al. Investigating the effect of coal particle size on spontaneous combustion and oxidation characteristics of coal. Sustainability, Vol. 29, 2020, pp. 161113-161122.
- [81] Zhao, Y., C. L. Wang, Y. F. Zhang, and Q. Liu. Experimental study of adsorption effects on shale permeability. Natural Resources Research, Vol. 28, 2019, pp. 1575-1586.
- [82] Zhao, Y., J. Bi, C. L. Wang, and P. F. Liu. Effect of unloading rate on the mechanical behavior and fracture characteristics of sandstones under complex triaxial stress conditions. Rock Mechanics and Rock Engineering, Vol. 54, 2021, pp. 4851-4866.
- [83] Zhao, Y. and H. H. Liu An elastic stress-strain relationship for porous rock under anisotropic stress conditions. Rock Mechanics and Rock Engineering, Vol. 45, 2012, pp. 389-399.
- Cui, L., N. Qin, S. Wang, and X. Z. Feng. Experimental study on the mechanical properties of sandstone under the action of chemical erosion and freeze-thaw cycles. Advances in Civil Engineering, Vol. 2021, 2021, id. 8884079.